

Real-space Formalism for the Euler Class and Fragile Topology in Quasicrystals and Amorphous Lattices

Dexin Li¹, Citian Wang¹ and Huaqing Huang^{1,2,3*}

¹ School of Physics, Peking University, Beijing 100871, China

² Collaborative Innovation Center of Quantum Matter, Beijing 100871, China

³ Center for High Energy Physics, Peking University, Beijing 100871, China

* huaqing.huang@pku.edu.cn

Abstract

We propose a real-space formalism of the topological Euler class, which characterizes the fragile topology of two-dimensional systems with real wave functions. This real-space description is characterized by local Euler markers whose macroscopic average coincides with the Euler number, and it applies equally well to periodic and open boundary conditions for both crystals and noncrystalline systems. We validate this by diagnosing topological phase transitions in clean and disordered crystalline systems with the reality endowed by the space-time inversion symmetry \mathcal{I}_{ST} . Furthermore, we demonstrated the topological Euler phases in quasicrystals and even in amorphous lattices lacking any spatial symmetries. Our work not only provides a local characterization of the fragile topology but also significantly extends its territory beyond \mathcal{I}_{ST} -symmetric crystalline materials.

Copyright attribution to authors.

This work is a submission to SciPost Physics.

License information to appear upon publication.

Publication information to appear upon publication.

Received Date

Accepted Date

Published Date

1

2 Contents

3	1 Introduction	2
4	2 Characteristic class in k- versus r-space	3
5	3 Remarks on r-space Euler number	4
6	4 Tight-binding model	5
7	5 Diagnosis of Topological phase transitions	5
8	6 Fragile topology in quasicrystals and amorphous lattices	8
9	7 Conclusion	9
10	A Orientability of our models	9
11	B Derivation of Eq. (4) in the main text	10

12	C Derivation of Eq. (6) in the main text	13
13	D Numerical implementation of the real-space Euler number	15
14	E The distinction between the real-space Chern and Euler numbers	16
15	F Averaging the local Euler marker in finite systems with OBC	17
16	G Brief discussion of the reality condition in \mathcal{PT}-broken systems	20
17	H Details of the model and method	20
18	H.1 Model	20
19	H.2 Disorder of on-site energy	20
20	H.3 Structural disorder	21
21	H.4 Twisted boundary condition for quasicrystals	21
22	H.5 Construction of composite Wannier function	21
23	H.6 Numerical calculation of the k-space Euler number	22
24	I More numerical results	22
25	I.1 Band structures around the topological phase transition in Fig. 1(b)	22
26	I.2 Convergence of the real-space Euler number with decreasing band gap	23
27	I.3 Convergence of the real-space Euler number with increasing lattice size	23
28	I.4 Local Euler markers in lattices with on-site disorder in Fig. 1(c)	24
29	I.5 Euler insulator in lattice with moderate structural disorder	27
30	I.6 Validation in other models with different Euler numbers	27
31	References	30
32		
33		

34 1 Introduction

35 Topological phases have garnered attention for their unique properties, originating with the
36 integer quantum Hall effect which is characterized by the topological invariant called the
37 Chern number [1–3] and associated chiral edge modes [4, 5]. Mathematically, the Chern
38 number is derived from the Chern class, a cohomology class characterizing *complex* vector
39 bundles. Typically, Chern numbers can be determined from complex Bloch wave functions via
40 a momentum-space expression that relies on the translation invariance of crystalline solids
41 [6–9]. However, in open-boundary systems, or in the presence of disorder, the lack of transi-
42 tional invariance renders the momentum-space expression no longer available. This has led
43 to the development of a real-space representation of the Chern number [10], including local
44 Chern markers [11, 12] and the nonlocal Bott index [13, 14], which triggers extensive study
45 on the real-space characterizations of more topological states of matter [15–41].

46 Recently, novel topological phases characterized by Euler and Stiefel-Whitney classes have
47 been proposed in orientable *real* vector bundles associated with real Bloch states [42–47].
48 Physically, two-dimensional real wave functions can be topologically classified by the Stiefel-
49 Whitney numbers [48–50] which are \mathbb{Z}_2 invariants taking either 0 or 1, and each two-band
50 subspace may exhibit a fragile topology that is characterized by an integer Euler number
51 $e \in \mathbb{Z}$ [51–53]. Similar to the Chern number, the Euler number can be expressed as an integral
52 in momentum space for real orientable two-band subsystems, and its parity is identical to the

53 second Stiefel-Whitney number w_2 , implying a close relationship between these two classes.
 54 Unlike the Chern insulator, the fragile topology of the Euler class can be tuned by adding triv-
 55 ial bands, implying its non-additive feature [49, 50]. Nevertheless, such a fragile topology
 56 protects the nonzero superfluid weight in twisted bilayer graphene [54]. Moreover, the Euler
 57 class also serves as non-Abelian topological invariants to characterize the band nodal braiding
 58 in multi-gap systems, which is in stark contrast to the single-gap Abelian topology within the
 59 ten-fold way classification [55]. Such multi-gap non-Abelian topology has been implemented
 60 in various systems such as crystalline materials [47, 56], acoustic metamaterials [57–59], and
 61 photonic systems [60–63], stimulating rapid recent progress in this ever-growing field [64–67].

62 Typically, the real Bloch states in crystals are enforced by the space-time inversion sym-
 63 metry \mathcal{I}_{ST} (time-reversal \mathcal{T} combined with inversion \mathcal{P} or two-fold rotation \mathcal{C}_{2z}) [68], which
 64 can be destroyed locally in the presence of disorder. Moreover, in a finite nonmagnetic sys-
 65 tem with open boundaries, \mathcal{I}_{ST} symmetry is not even essential for the reality condition. The
 66 limitation of the momentum-space formula makes it urgent to search for a local characteriza-
 67 tion of real topological phases in systems with disorder and more generally in open-boundary
 68 systems inherently lacking translation and \mathcal{I}_{ST} symmetries, such as quasicrystals [69–74] and
 69 amorphous systems [75–80].

70 In this Letter, we develop a real-space formalism for Euler class topology in 2D systems.
 71 In an analogy to the Chern class, we introduce a local Euler marker $e(\mathbf{r})$ to directly map the
 72 Euler topology in real space for both crystals and noncrystalline systems. The macroscopic
 73 average of $e(\mathbf{r})$ coincides with the Euler number regardless of periodic or open boundary
 74 conditions. We validate our real-space formalism by verifying topological Euler and trivial
 75 phases in clean systems, yielding consistent results with \mathbf{k} -space approaches. Additionally, we
 76 apply our method to a particular \mathcal{PT} -symmetric disordered system, successfully diagnosing the
 77 disorder-induced topological phase transition. Furthermore, our real-space formalism proves
 78 powerful in characterizing fragile topological phases in quasicrystals and even in amorphous
 79 systems lacking any spatial symmetries.

80 2 Characteristic class in \mathbf{k} - versus \mathbf{r} -space

81 The Euler class is a characteristic class of oriented real vector bundles. It can be constructed us-
 82 ing an orthonormal basis $\{|u_n(\mathbf{k})\rangle\}$, where $|u_n(\mathbf{k})\rangle$ represents the cell-periodic part of the n -th
 83 occupied Bloch state $\langle \mathbf{r} | \psi_n(\mathbf{k}) \rangle = e^{i\mathbf{k}\cdot\mathbf{r}} \langle \mathbf{r} | u_n(\mathbf{k}) \rangle$. Utilizing this basis, we obtain the curvature
 84 matrix \mathcal{F} with its entries given by:

$$\mathcal{F}_{mn}(\mathbf{k}) = \langle \partial_{[k_x} u_m(\mathbf{k}) | \partial_{k_y]} u_n(\mathbf{k}) \rangle dk_x \wedge dk_y, \quad (1)$$

85 where $[\dots, \dots]$ denotes the commutator applied to the index k_x and k_y . When there are two
 86 occupied bands, the Euler class can be expressed as a differential 2-form in \mathbf{k} space,

$$\begin{aligned} e(\mathcal{F}) &= \frac{1}{2\pi} \text{Pf}(\mathcal{F}), \\ &= \frac{1}{2\pi} \langle \partial_{[k_x} u_1(\mathbf{k}) | \partial_{k_y]} u_2(\mathbf{k}) \rangle dk_x \wedge dk_y, \end{aligned} \quad (2)$$

87 where Pf denotes the Pfaffian acting on the matrix \mathcal{F} . The Euler number e is an integer topo-
 88 logical invariant for two real bands, which can be expressed as a simple \mathbf{k} -space integral [81],

$$e = \frac{1}{2\pi} \int_{BZ} \langle \partial_{[k_x} u_1(\mathbf{k}) | \partial_{k_y]} u_2(\mathbf{k}) \rangle dk_x dk_y. \quad (3)$$

89 To derive the expression of the Euler number in \mathbf{r} -space, we start by replacing the occupied
 90 states in the above expression with a projection operator $\hat{P}(\mathbf{k}) = \sum_{\text{occ}} |u_n(\mathbf{k})\rangle \langle u_n(\mathbf{k})|$ in the

91 occupied subspace [11]. After some algebra (see appendix B), we obtain the \mathbf{k} -space formula
 92 of Euler number e represented by $\hat{P}(\mathbf{k})$,

$$e = \frac{1}{2\pi} \int_{BZ} d^2\mathbf{k} \text{Pf}_{\text{occ}}(\hat{P}(\mathbf{k})[\partial_{k_x}\hat{P}(\mathbf{k}), \partial_{k_y}\hat{P}(\mathbf{k})]), \quad (4)$$

93 where Pf_{occ} denotes the Pfaffian taken over the occupied subspace. Then we can straightfor-
 94 wardly generalize it from \mathbf{k} to \mathbf{r} space via the duality (see appendix C),

$$\begin{aligned} \int_{BZ} \frac{d^2\mathbf{k}}{(2\pi)^2/A} &\rightarrow \text{Tr} \\ \partial_{k_x}\hat{P}(\mathbf{k}) &\rightarrow \frac{L_x}{2\pi}(\hat{U}\hat{P}\hat{U}^\dagger - \hat{P}), \\ \partial_{k_y}\hat{P}(\mathbf{k}) &\rightarrow \frac{L_y}{2\pi}(\hat{V}\hat{P}\hat{V}^\dagger - \hat{P}), \end{aligned} \quad (5)$$

95 where $A = L_x L_y$ is the area of the system, $\hat{U} = \exp(2\pi i \hat{X}/L_x)$ and $\hat{V} = \exp(2\pi i \hat{Y}/L_y)$ are the
 96 unitary position operator, Tr is the trace over the coordinate space, and \hat{P} is the \mathbf{r} -space projec-
 97 tion operator. Note that the order of \hat{P} is determined by both the site coordinates $\mathbf{r}_i = (x_i, y_i)$,
 98 dependent on the lattice size, and the internal index n , matching the order of $\hat{P}(\mathbf{k})$. Therefore,
 99 we can divide the space on which \hat{P} operates into two subspaces, $S(\hat{P}) = l^2(\mathbb{T}^2) \otimes \mathbb{R}^N$. Here,
 100 $l^2(\mathbb{T}^2)$ is the coordinate space, where \mathbb{T}^2 denotes the two-torus, a rectangle with edge length
 101 L_x and L_y with periodic boundary conditions (PBC) [14]. And \mathbb{R}^N is internal space with the
 102 internal degrees of freedom N which are those degrees of freedom except for the coordinate
 103 \mathbf{k} or $\{\mathbf{r}_i\}$. Consequently, we arrive at the \mathbf{r} -space expression for the Euler number:

$$e = \frac{1}{2\pi} \text{Tr} \text{Pf}_{\text{occ}}(\hat{P}[\hat{U}\hat{P}\hat{U}^\dagger, \hat{V}\hat{P}\hat{V}^\dagger]), \quad (6)$$

104 where Pf_{occ} denotes the Pfaffian taken over the occupied submatrix in the internal space (see
 105 appendix D for more details). Analogous to prior work on the local Chern marker [11], we
 106 propose defining the local Euler marker $e(\mathbf{r})$ as the expression in Eq. (6) before taking the
 107 trace, i.e.,

$$e(\mathbf{r}) = \frac{1}{2\pi} \text{Pf}_{\text{occ}}(\langle \mathbf{r} | \hat{P}[\hat{U}\hat{P}\hat{U}^\dagger, \hat{V}\hat{P}\hat{V}^\dagger] | \mathbf{r} \rangle). \quad (7)$$

108 The \mathbf{r} -space Euler number (6) and local Euler marker (7) apply well to both crystalline and
 109 noncrystalline systems. They not only provide an intuitive local perspective of global topology
 110 but also serve as a valuable tool for distinguishing topological phases in aperiodic systems
 111 without translational symmetry.

112 3 Remarks on \mathbf{r} -space Euler number

113 Before proceeding, we have a few remarks. First, the analysis we've conducted thus far can
 114 be directly applied to the Chern class, and the resultant \mathbf{r} -space expression is nothing but
 115 the Bott index, $\text{Bott}(\hat{U}, \hat{V}) = (1/2\pi) \text{Im} \text{Tr} \log(\hat{U}\hat{V}\hat{U}^{-1}\hat{V}^{-1})$ with $\hat{U} = \hat{P} \exp(2\pi i \hat{X}/L_x) \hat{P}$ and
 116 $\hat{V} = \hat{P} \exp(2\pi i \hat{Y}/L_y) \hat{P}$, which offers an equivalent topological classification to the Chern num-
 117 ber [14, 15]. However, there are significant differences between the \mathbf{r} -space formulation of the
 118 Euler and Chern number. The \mathbf{r} -space Chern number only requires a simple trace performed
 119 consistently in both coordinate and internal space. In contrast, for the \mathbf{r} -space Euler number,
 120 it becomes essential to distinguish between the coordinate and internal space, which requires
 121 trace and Pfaffian operations, respectively.

122 Secondly, to decompose the coordinate and internal spaces for extracting the occupied sub-
 123 matrix needed for Pfaffian calculation, we apply a unitary transformation to the eigenstates
 124 which makes \hat{P} block-diagonal. This unitary transformation corresponds to constructing a set
 125 of composite Wannier functions, which can be determined by an explicit algorithm of localiza-
 126 tion functional minimization proposed by Marzari and Vanderbilt [82, 83] (see appendix H.5).
 127 Importantly, while a nontrivial topological invariant may pose a topological obstruction for
 128 constructing Wannier representations composed of exponentially localized states in line with
 129 lattice symmetries [49, 51, 84, 85], it does not hinder the search for composite Wannier func-
 130 tions with optimal power-law decay [86–91].

131 Thirdly, the distinct treatments of Chern and Euler numbers in real space also lead to
 132 different behaviors in finite samples under open boundary conditions (OBC). It's well-known
 133 that the summation of the local Chern marker over an entire open system must equal zero,
 134 regardless of whether the system is a Chern insulator or not. This is because the local Chern
 135 marker in the bulk is always offset by the significant deviation at the boundary [11, 14]. In
 136 contrast, the local Euler marker near the open boundary fades away and thus doesn't suffer
 137 from the counteraction under OBC, making the choice of boundary condition irrelevant for
 138 the \mathbf{r} -space Euler number (see appendix E).

139 4 Tight-binding model

140 To numerically validate the \mathbf{r} -space formula of Euler number, we consider a general \mathcal{PT} -
 141 symmetric tight-binding model with the basis $(ip_x, ip_y, d_{xy}, d_{x^2-y^2})$ per site. The Hamiltonian
 142 is given by

$$H = \sum_{i\mu} \epsilon_\mu c_{i\mu}^\dagger c_{i\mu} + \sum_{\langle ij \rangle} \sum_{\mu\nu} t_{\mu\nu}(\mathbf{r}_{ij}) c_{i\mu}^\dagger c_{j\nu}, \quad (8)$$

143 where $c_{i\mu}^\dagger$ ($c_{i\mu}$) is electron creation (annihilation) operator on the μ orbital at the i -th site. ϵ_μ is
 144 the on-site energy and $t_{\mu\nu}(\mathbf{r}_{ij})$ is the Slater-Koster parameterized hopping integral [92, 93] and
 145 has an inverse-square decay with the distance (i.e., $|\mathbf{r}_{ij}|^{-2}$) [94]. It has been proven that a \mathcal{PT} -
 146 symmetric Hamiltonian can become real-valued through the Takagi decomposition [49, 95].
 147 Here we intentionally chose the p orbitals to be imaginary, which results in $\mathcal{PT} = \hat{K}$ with the
 148 complex conjugation operator \hat{K} . The invariance of the Hamiltonian under \mathcal{PT} imposes the
 149 reality condition on H . It was previously known that a fragile topological state with a nontrivial
 150 Euler number $e = 1$ can be achieved by considering a double band inversion between $p_{x,y}$
 151 and $d_{x^2-y^2,xy}$ orbitals [96]. Here we verify the validity of the \mathbf{r} -space Euler number in both
 152 crystalline and noncrystalline systems based on this model. We also validate our expression
 153 using other models with different Euler numbers, which are detailed in the appendix I.6.

154 5 Diagnosis of Topological phase transitions

155 With the well-defined \mathbf{r} -space Euler number, we first diagnose topological phase transitions in
 156 a square lattice based on the model in Eq. (8). As shown in Fig. 1(a), the orbital-resolved band
 157 structure displays signs of a double band inversion between $p_{x,y}$ and $d_{x^2-y^2,xy}$ orbitals around
 158 the Γ point, implying their nontrivial electronic topology. We compute the Euler number in
 159 both \mathbf{k} -space and \mathbf{r} -space, consistently yielding a value of $e = 1$, thus confirming the nontrivial
 160 Euler topology. We further examine the evolution of the Euler number in both \mathbf{k} - and \mathbf{r} -
 161 spaces with increasing the on-site energy difference $\Delta = \epsilon_p - \epsilon_d$. In Fig. 1(b), the system
 162 undergoes a topological phase transition from a topological Euler insulator with $e = 1$ (region
 163 I) to an intermediate gapless state (II) and eventually transitions into a trivial insulator with

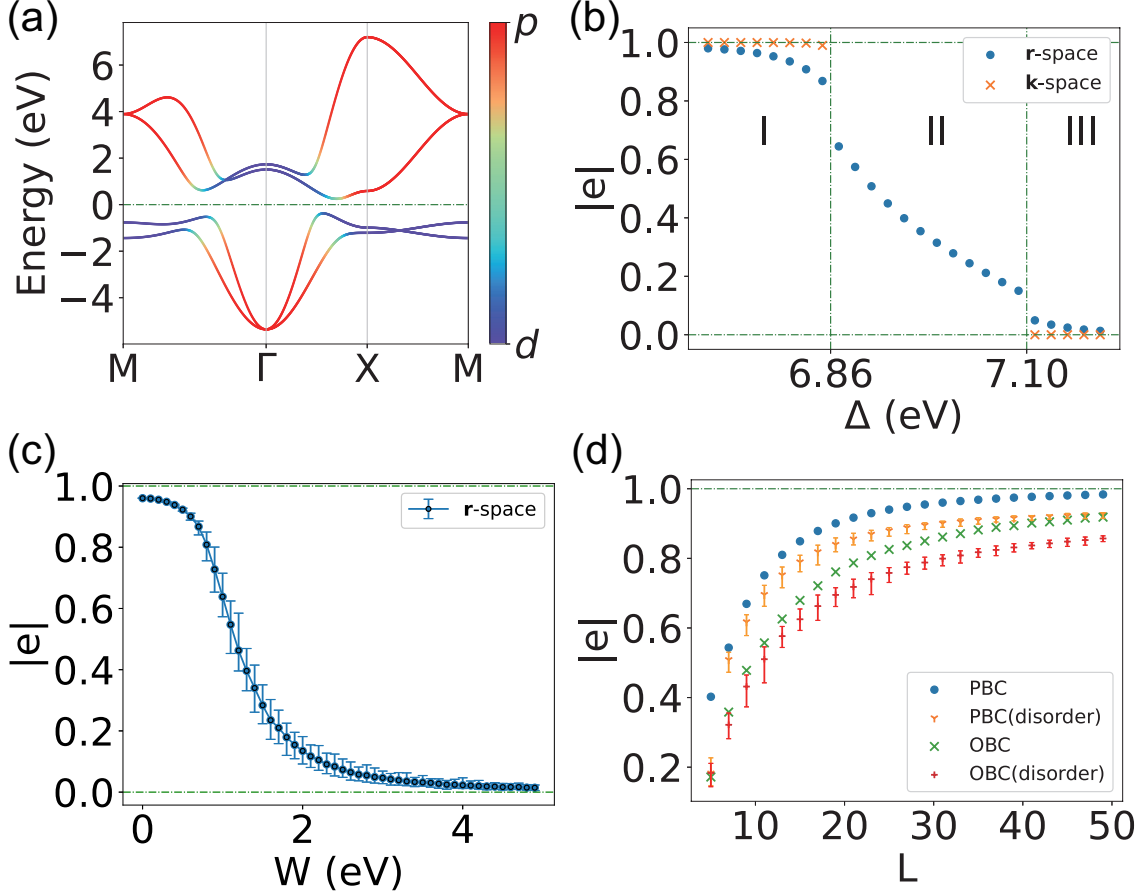


Figure 1: (a) Orbital-resolved band structures of the square lattice with a double band inversion between $p_{x,y}$ and $d_{x^2-y^2,xy}$ orbitals. The parameters used are $\epsilon_{p_x,p_y} = 1.58$, $\epsilon_{d_{x^2-y^2,xy}} = -0.42$, $V_{pp\sigma} = -0.865$, $V_{pp\pi} = -0.144$, $V_{pd\sigma} = 0.173$, $V_{pd\pi} = 0.135$, $V_{dd\sigma} = 0.144$, $V_{dd\pi} = 0.124$, $V_{dd\delta} = 0.259$ eV. (b) The variation of the Euler number as the on-site energy difference $\Delta = \epsilon_p - \epsilon_d$ changes. Other parameters remain unchanged and the lattice size is $L = 201$. (c) The r -space Euler number as a function of the disorder strength W in 31×31 square lattices with periodic boundary condition (PBC). (d) The lattice size L dependence of the r -space Euler number calculated without and with on-site energy disorder ($W = 1.0$ eV) using PBC and open boundary condition (OBC). For each L and W , the configuration average is performed over 100 realizations.

164 $e = 0$ (III). The calculated \mathbf{r} -space Euler number matches with the \mathbf{k} -space one, except for the
 165 intermediate gapless phase (region II) where the Euler number is ill-defined. This transition
 166 can be understood by tracing the evolution of band inversion (see appendix I.1): Starting
 167 from a double inverted band order, the nontrivial energy gap gradually decreases to zero with
 168 increasing Δ , then remains closed over a finite Δ range, and eventually reopens with a trivial
 169 normal band order.

170 Next, we demonstrate the applicability of the \mathbf{r} -space Euler number for aperiodic sys-
 171 tems by introducing the disorder term in the on-site energies of the aforementioned model.
 172 We specifically consider disorder term that preserves \mathcal{PT} symmetry, which is represented by
 173 $V_{\text{dis}} = \sum_{i \in \tau_{1/2}} \lambda_i (c_i^\dagger c_i + c_{\mathcal{P}i}^\dagger c_{\mathcal{P}i})$ with the random variables $\{\lambda_i\}$ distributed uniformly within the
 174 interval $[-W, W]$ on half of the sites ($\tau_{1/2}$) in the sample, where W is the disorder strength.
 175 The annihilation operators c_i and $c_{\mathcal{P}i}$ act on the site at \mathbf{r}_i and its inversion partner $\mathcal{P}\mathbf{r}_i$, respec-
 176 tively. The averaged \mathbf{r} -space Euler number as a function of W is shown in Fig. 1(c). For mod-
 177 erate disorder, the \mathbf{r} -space Euler number e remains around 1, indicating the system remains
 178 topologically nontrivial. Remarkably, as disorder strength W increases, e gradually decreases
 179 to 0, diagnosing a topological phase transition (see appendix I.4). Our results confirm the
 180 disorder-induced topological phase transition classified by the topological Euler class [97, 98],
 181 and validate the \mathbf{r} -space formalism of Euler number in disordered systems.

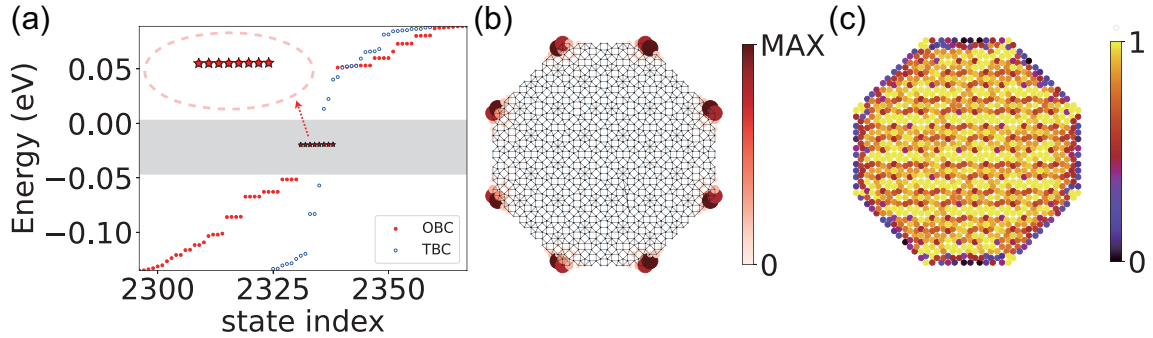


Figure 2: Fragile topological state characterized by $e = 1$ in the Ammann-Beenker tiling quasicrystal based on the model in Eq. (8). Parameters are $\epsilon_{p_x, p_y} = 1.58$, $\epsilon_{d_x^2 - y^2, x_y} = -0.42$, $V_{pp\sigma} = -1.783$, $V_{pp\pi} = -0.299$, $V_{pd\sigma} = 0.359$, $V_{pd\pi} = 0.280$, $V_{dd\sigma} = 0.299$, $V_{dd\pi} = 0.257$, $V_{dd\delta} = 0.537$ eV. (a) Energy spectrum of the quasicrystal containing 1168 sites with OBC or twisted boundary condition (TBC). Insert shows 8 corner states (highlighted by red stars) in the bulk gap. (b) Spatial distribution of the in-gap corner states [red stars in (a)]. (c) The distribution of local Euler markers $e(\mathbf{r})$ in the quasicrystal with OBC.

182 We further check the effect of lattice size and different boundary conditions on the \mathbf{r} -
 183 space Euler number, as shown in Fig. 1(d). All calculated \mathbf{r} -space Euler numbers converge
 184 to the limit of 1 with different rates by increasing the lattice size, demonstrating the faithful
 185 formalism of the Euler number. Importantly, the OBC results exhibit a deviation from PBC
 186 due to the presence of open boundaries, but this difference can be diminished by increasing
 187 lattice size or averaging the local Euler marker $e(\mathbf{r})$ only in the inner area of the sample (see
 188 appendix ??).

189 This suggests that the \mathbf{r} -space formula remains reliable regardless of the boundary condi-
 190 tions, which is notably different from the Chern number.

191 It is also noted that the disordered case converges much slower than the pristine PBC case.
 192 Because the disordered system is close to the critical point, the energy gap reduces signifi-
 193 cantly and the correlation length increases, which demands larger lattice sizes for accurate
 194 calculations of the real-space Euler number⁰. Our results show that the \mathbf{r} -space Euler number

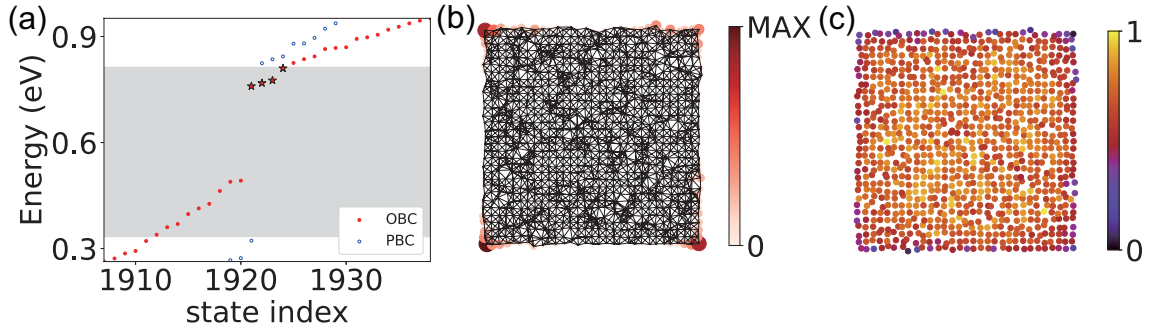


Figure 3: Fragile topological state characterized by $e = 1$ in the amorphous square lattice based on the model in Eq. (8). Parameters are $L=31$, $\epsilon_{p_x, p_y} = 1.58$, $\epsilon_{d_x^2-y^2, xy} = -0.42$, $V_{pp\sigma} = -0.565$, $V_{pp\pi} = -0.044$, $V_{pd\sigma} = 0.773$, $V_{pd\pi} = 0.335$, $V_{dd\sigma} = 0.444$, $V_{dd\pi} = 0.224$, $V_{dd\delta} = 0.659$ eV. (a) Energy spectrum of the amorphous square lattice with PBC and OBC. Four corner states in the gap are highlighted by red stars. (b) Spatial distribution of the corner states [red stars in (a)]. (c) The distribution of $e(\mathbf{r})$ for the amorphous system with OBC.

195 equals the exact one within a correction of order $\mathcal{O}(1/(L\Delta E))$ for systems with lattice size L
 196 and energy gap ΔE , which resembles the case of Bott index and Chern number [14].

197 6 Fragile topology in quasicrystals and amorphous lattices

198 As an application of our proposed \mathbf{r} -space formula, we explore the Euler topology in qua-
 199 sicrystals and amorphous lattices. Specifically, we consider the 2D Ammann-Beenker-tiling
 200 quasicrystal, which possesses 8-fold rotational symmetry but lacks translational symmetry. In
 201 the finite octagonal quasicrystal sample with open boundary conditions (OBC), 8 degenerate
 202 states emerge within the bulk gap region (grey area), as shown in Fig. 2(a). The bulk gap
 203 estimation utilizes a twisted boundary condition (TBC) to preserve octagonal symmetry and
 204 eliminate boundary effects (see appendix H.4). We plot the spatial distribution of these in-gap
 205 states [see Fig. 2(b)], and find that they are well localized at 8 corners of the octagonal qua-
 206 sicrystal, implying its feature of higher-order topology. We also examine the local Euler marker
 207 distribution in the finite quasicrystal sample, as depicted in Fig. 2(c). The plot confirms that
 208 the local Euler markers $e(\mathbf{r})$ closely match the expected value of 1 within the bulk but deviate
 209 at the edges. As expected, the average of $e(\mathbf{r})$ over the entire finite sample does not vanish
 210 but yields $e \approx 1$, verifying the nontrivial Euler topology of the quasicrystal.

211 We further study a finite amorphous lattice constructed by assigning random site displace-
 212 ments away from their equilibrium position in an initial square lattice. Consequently, all spatial
 213 symmetries are broken, including \mathcal{P} or \mathcal{C}_{2z} demanded by \mathcal{I}_{ST} symmetry for real Bloch states in
 214 periodic crystals. Nevertheless, for the spinless model (8) in any amorphous lattice with OBC,
 215 it is always possible to choose a real gauge so that both the Hamiltonian and eigenstates can
 216 be taken real (see appendix G). This implies that the \mathbf{r} -space Euler number is still applicable to
 217 identify its Euler topology. As shown in Fig. 3(a), the energy spectrum of the finite amorphous
 218 lattice with OBC exhibits 4 corner states at the Fermi level in the bulk gap estimated using
 219 artificial PBC (grey area). The spatial distribution of these states supports that they are indeed
 220 localized at 4 corners of the finite sample [see Fig. 3(b)]. As shown in Fig. 3(c), local Euler
 221 markers $e(\mathbf{r})$ are dominated in the internal area but tend to vanish at the boundary of the finite
 222 amorphous sample. The sum of $e(\mathbf{r})$ over the entirety of the finite sample yields a nonzero
 223 Euler number which is expected to converge to the quantized value of 1 with increasing lattice

224 size.

225 7 Conclusion

226 We have proposed an explicit real-space formula for the Euler number to identify the fragile
 227 topological phases in both crystalline and noncrystalline systems whose wave functions are
 228 real. Specifically, the local Euler marker $e(\mathbf{r})$ whose macroscopic average coincides with the
 229 Euler number e , is introduced to characterize the topological order in real space. Notably,
 230 this applies equally well to periodic and open boundary conditions. We have validated our
 231 expression by diagnosing the topological phase transition in crystals and disordered systems
 232 with \mathcal{PT} symmetry. Furthermore, we have also uncovered the topological Euler phases in
 233 quasicrystals and amorphous lattices without any spatial symmetry. Our work greatly extends
 234 the concept of real-space topological markers to topological states in real Hilbert space and
 235 would hopefully inspire future exploration in more topological characteristic classes in real
 236 space.

237 Acknowledgements

238 We thank Guo Chuan Thiang for the valuable discussions.

239 **Author contributions** D.L. and C.W. contributed equally to this work.

240 **Funding information** This work is supported by the National Key R&D Program of China
 241 (Grant No. 2021YFA1401600) and the National Natural Science Foundation of China (Grant
 242 No. 12074006). The computational resources were supported by the high-performance com-
 243 puting platform of Peking University.

244 A Orientability of our models

245 In this section, we examine the orientability of our models. The Euler class $\epsilon(\mathcal{F})$ is defined as

$$\epsilon(\mathcal{F}) = \frac{1}{2\pi} \text{Pf}(\mathcal{F}), \quad (\text{A.1})$$

246 where Pf denotes the Pfaffian acting on the curvature matrix \mathcal{F} . Under the basis transformation
 247 O , the Euler class acquires an additional factor $\det(O)$, as shown below:

$$\begin{aligned} \epsilon(\mathcal{F}) &\rightarrow \epsilon(O^{-1}\mathcal{F}O), \\ &= \frac{1}{2\pi} \text{Pf}(O^{-1}\mathcal{F}O), \\ &= \frac{1}{2\pi} \text{Pf}(O^T\mathcal{F}O), \end{aligned} \quad (\text{A.2})$$

248 where the last equality originates from the orthonormality property of the real wave functions,
 249 which means $O^{-1} = O^T$. It's worth noting that for a $2n \times 2n$ skew-symmetric matrix A and an
 250 arbitrary $2n \times 2n$ matrix B , the Pfaffian satisfies the identity $\text{Pf}(B^T A B) = \text{Pf}(A) \det(B)$. There-
 251 fore, since the curvature matrix \mathcal{F} is skew-symmetric, we can simplify the expression further

252 as:

$$\begin{aligned}\epsilon(\mathcal{F}) &\rightarrow \frac{1}{2\pi} \text{Pf}(\mathcal{F}) \det(O), \\ &= \epsilon(\mathcal{F}) \det(O).\end{aligned}\tag{A.3}$$

253 For the Euler class $\epsilon(\mathcal{F})$ to be a characteristic class, it must remain invariant under any basis
254 transformation. Therefore, a certain transformation matrix O with $\det(O) = 1$ is essential.
255 Since O is the transformation matrix between orthonormal basis, it naturally satisfies the con-
256 dition $|\det(O)|=1$. Thus, system orientability is necessary to prevent $\det(O) = -1$ and ensure
257 the invariance of the Euler class.

258 In fact, the orientability of the Brillouin zone is determined by the first Stiefel-Whitney
259 class w_1 , which is the total Berry phase of the occupied states over the Brillouin zone [45].
260 Because the Chern number of a time-reversal symmetric system is always trivial, a complex
261 smooth gauge can be found in this system. Given a Berry connection A that satisfies $\mathcal{F} = dA$
262 in this gauge, we have

$$w_1|_C = \frac{1}{\pi} \oint_C d\mathbf{k} \cdot \text{Tr}A(\mathbf{k}).\tag{A.4}$$

263 Therefore, our models are easily confirmed to be orientable with a trivial $w_1 = 0$, allowing us
264 to proceed with our discussion on the Euler class and the second Stiefel-Whitney class.

265 B Derivation of Eq. (4) in the main text

266 In this section, we derive Eq. (4) in the main text, beginning with the relation between the
267 Chern and Euler class in a two-dimensional system. Specifically, there is a correspondence
268 between the first Chern class c_1 and the Euler class ϵ :

$$c_1(\mathcal{F}_C) = \epsilon(\mathcal{F}),\tag{B.1}$$

269 where \mathcal{F}_C is the curvature over a complex number field, isomorphic to \mathcal{F} over a real number
270 field through an isomorphism $\mathbb{C} \cong \mathbb{R} \oplus \mathbb{R}$. In particular, for a system with two occupied bands
271 ($N_{\text{occ}} = 2$), we can construct a complex Bloch state

$$|u\rangle = \frac{1}{\sqrt{2}}(|u_1\rangle + i|u_2\rangle),\tag{B.2}$$

272 where $|u_n\rangle$ ($n = 1, 2$) represents the cell-periodic part of the n -th occupied Bloch state $|\psi_n(\mathbf{k})\rangle$.
273 Note that for brevity, we omit the explicit dependence of \mathbf{k} in this section for $|u_n(\mathbf{k})\rangle$, $|u(\mathbf{k})\rangle$,
274 and the projection operator $\tilde{P}(\mathbf{k})$. Based on the complex Bloch states, the first Chern class is
275 given by

$$c_1(\mathcal{F}_C) = \frac{1}{2\pi i} \mathcal{F}_C = \frac{1}{2\pi i} \langle \partial_{[k_x} u | \partial_{k_y]} u \rangle dk_x \wedge dk_y.\tag{B.3}$$

276 This allows us to derive the expression of the Euler class from the first Chern class.

277 To begin with, we can express the first Chern number as a \mathbf{k} -space integral:

$$c_1 = \frac{1}{2\pi i} \int_{BZ} d^2\mathbf{k} \text{Tr}(\tilde{P} \partial_{[k_x} \tilde{P} \partial_{k_y]} \tilde{P}),\tag{B.4}$$

278 where the integral is over the Brillouin zone (BZ) and $\tilde{P} = |u\rangle\langle u|$ is the projection operator,
279 with its real and imaginary parts given by:

$$\text{Re}\tilde{P} = \frac{1}{2}(|u_1\rangle\langle u_1| + |u_2\rangle\langle u_2|)\tag{B.5}$$

280 and

$$\text{Im}\tilde{P} = \frac{1}{2}(|u_2\rangle\langle u_1| - |u_1\rangle\langle u_2|). \quad (\text{B.6})$$

281 Using Eq. (B.2), we can rewrite Eq. (B.4) as

$$c_1 = \frac{1}{2\pi i} \int_{BZ} d^2\mathbf{k} \langle u | [\partial_{k_x} \tilde{P}, \partial_{k_y} \tilde{P}] | u \rangle, \quad (\text{B.7})$$

282 and then the Euler number is given by

$$\begin{aligned} e &= \frac{1}{4\pi i} \int_{BZ} d^2\mathbf{k} \langle u_1 | [\partial_{k_x} \tilde{P}, \partial_{k_y} \tilde{P}] | u_1 \rangle + \frac{1}{4\pi i} \int_{BZ} d^2\mathbf{k} \langle u_2 | [\partial_{k_x} \tilde{P}, \partial_{k_y} \tilde{P}] | u_2 \rangle \\ &+ \frac{1}{4\pi} \int_{BZ} d^2\mathbf{k} \langle u_1 | [\partial_{k_x} \tilde{P}, \partial_{k_y} \tilde{P}] | u_2 \rangle - \frac{1}{4\pi} \int_{BZ} d^2\mathbf{k} \langle u_2 | [\partial_{k_x} \tilde{P}, \partial_{k_y} \tilde{P}] | u_1 \rangle. \end{aligned} \quad (\text{B.8})$$

283 To keep the Euler number e real, we can simplify the operators $[\partial_{k_x} \tilde{P}, \partial_{k_y} \tilde{P}]$ in Eq. (B.8) to

$$i[\partial_{k_x} \text{Re}\tilde{P}, \partial_{k_y} \text{Im}\tilde{P}] + i[\partial_{k_x} \text{Im}\tilde{P}, \partial_{k_y} \text{Re}\tilde{P}] \quad (\text{B.9})$$

284 for the first two terms and

$$[\partial_{k_x} \text{Re}\tilde{P}, \partial_{k_y} \text{Re}\tilde{P}] - [\partial_{k_x} \text{Im}\tilde{P}, \partial_{k_y} \text{Im}\tilde{P}] \quad (\text{B.10})$$

285 for the other terms. Since $\{|u_n\rangle\}$ are orthonormal, we have the following identities:

$$\langle u_n | u_m \rangle = \delta_{n,m} \quad (\text{B.11})$$

286 and

$$\langle u_n | \partial_{k_i} u_n \rangle = \frac{1}{2} \partial_{k_i} (\langle u_n | u_n \rangle) = 0. \quad (\text{B.12})$$

287 Therefore, we have

$$\begin{cases} \partial_{k_i} \text{Re}\tilde{P} | u_1 \rangle = \frac{1}{2} (|\partial_{k_i} u_1\rangle + |u_2\rangle\langle u_1 | \partial_{k_i} u_2 \rangle) \\ \partial_{k_i} \text{Re}\tilde{P} | u_2 \rangle = \frac{1}{2} (|\partial_{k_i} u_2\rangle - |u_1\rangle\langle u_1 | \partial_{k_i} u_2 \rangle) \\ \partial_{k_i} \text{Im}\tilde{P} | u_1 \rangle = \frac{1}{2} (|\partial_{k_i} u_2\rangle - |u_1\rangle\langle u_1 | \partial_{k_i} u_2 \rangle) = \partial_{k_i} \text{Re}\tilde{P} | u_2 \rangle \\ \partial_{k_i} \text{Im}\tilde{P} | u_2 \rangle = -\frac{1}{2} (|\partial_{k_i} u_1\rangle + |u_2\rangle\langle u_1 | \partial_{k_i} u_2 \rangle) = -\partial_{k_i} \text{Re}\tilde{P} | u_1 \rangle, \end{cases} \quad (\text{B.13})$$

288 with k_i denoting k_x or k_y . Since $\text{Re}\tilde{P}$ is a Hermitian operator and $\text{Im}\tilde{P}$ is an anti-Hermitian
289 operator, we have:

$$\langle u_n | \partial_{k_i} \text{Re}\tilde{P} = (\partial_{k_i} \text{Re}\tilde{P} | u_n \rangle)^\dagger \quad (\text{B.14})$$

290 and

$$-\langle u_n | \partial_{k_i} \text{Im}\tilde{P} = (\partial_{k_i} \text{Im}\tilde{P} | u_n \rangle)^\dagger, \quad (\text{B.15})$$

291 where the additional minus sign in Eq. (B.15) can be canceled by the minus sign in the com-
292 mutators in Eq. (B.9) and Eq. (B.10).

293 Therefore, the first term in Eq. (B.8) is

$$\begin{aligned}
& \frac{1}{4\pi i} \int_{BZ} d^2\mathbf{k} \langle u_1 | [\partial_{k_x} \tilde{P}, \partial_{k_y} \tilde{P}] | u_1 \rangle \\
&= \frac{1}{4\pi} \int_{BZ} d^2\mathbf{k} \langle u_1 | ([\partial_{k_x} \text{Re}\tilde{P}, \partial_{k_y} \text{Im}\tilde{P}] + [\partial_{k_x} \text{Im}\tilde{P}, \partial_{k_y} \text{Re}\tilde{P}]) | u_1 \rangle \\
&= \frac{1}{2\pi} \int_{BZ} d^2\mathbf{k} (\langle u_1 | \partial_{k_x} \text{Re}\tilde{P} \partial_{k_y} \text{Im}\tilde{P} | u_1 \rangle - \langle u_1 | \partial_{k_y} \text{Re}\tilde{P} \partial_{k_x} \text{Im}\tilde{P} | u_1 \rangle) \\
&= \frac{1}{2\pi} \int_{BZ} d^2\mathbf{k} (\langle u_1 | \partial_{k_x} \text{Re}\tilde{P} \partial_{k_y} \text{Re}\tilde{P} | u_2 \rangle - \langle u_1 | \partial_{k_y} \text{Re}\tilde{P} \partial_{k_x} \text{Re}\tilde{P} | u_2 \rangle) \\
&= \frac{1}{2\pi} \int_{BZ} d^2\mathbf{k} \langle u_1 | [\partial_{k_x} \text{Re}\tilde{P}, \partial_{k_y} \text{Re}\tilde{P}] | u_2 \rangle. \tag{B.16}
\end{aligned}$$

294 The analysis of the second term in Eq. (B.8) is similar, with the only difference being an addi-
 295 tional minus sign from Eq. (B.15) as

$$\begin{aligned}
& \frac{1}{4\pi i} \int_{BZ} d^2\mathbf{k} \langle u_2 | [\partial_{k_x} \tilde{P}, \partial_{k_y} \tilde{P}] | u_2 \rangle \\
&= -\frac{1}{2\pi} \int_{BZ} d^2\mathbf{k} \langle u_2 | \partial_{k_x} \text{Re}\tilde{P} \partial_{k_y} \text{Re}\tilde{P} | u_1 \rangle \\
&= \frac{1}{2\pi} \int_{BZ} d^2\mathbf{k} \langle u_1 | [\partial_{k_x} \text{Re}\tilde{P}, \partial_{k_y} \text{Re}\tilde{P}] | u_2 \rangle, \tag{B.17}
\end{aligned}$$

296 where the last equality holds due to the Hermiticity of $\text{Re}\tilde{P}$ and the reality of $|u_n\rangle$. Now, let's
 297 consider the third term in Eq. (B.8), which is

$$\begin{aligned}
& \frac{1}{4\pi} \int_{BZ} d^2\mathbf{k} \langle u_1 | [\partial_{k_x} \tilde{P}, \partial_{k_y} \tilde{P}] | u_2 \rangle \\
&= \frac{1}{4\pi} \int_{BZ} d^2\mathbf{k} (\langle u_1 | [\partial_{k_x} \text{Re}\tilde{P}, \partial_{k_y} \text{Re}\tilde{P}] | u_2 \rangle - \langle u_1 | [\partial_{k_x} \text{Im}\tilde{P}, \partial_{k_y} \text{Im}\tilde{P}] | u_2 \rangle) \\
&= \frac{1}{4\pi} \int_{BZ} d^2\mathbf{k} (\langle u_1 | [\partial_{k_x} \text{Re}\tilde{P}, \partial_{k_y} \text{Re}\tilde{P}] | u_2 \rangle - \langle u_2 | [\partial_{k_x} \text{Re}\tilde{P}, \partial_{k_y} \text{Re}\tilde{P}] | u_1 \rangle) \\
&= \frac{1}{2\pi} \int_{BZ} d^2\mathbf{k} \langle u_1 | [\partial_{k_x} \text{Re}\tilde{P}, \partial_{k_y} \text{Re}\tilde{P}] | u_2 \rangle. \tag{B.18}
\end{aligned}$$

298 Likewise, the final term in Eq. (B.8) can be expressed as:

$$\frac{1}{2\pi} \int_{BZ} d^2\mathbf{k} \langle u_1 | [\partial_{k_x} \text{Re}\tilde{P}, \partial_{k_y} \text{Re}\tilde{P}] | u_2 \rangle, \tag{B.19}$$

299 due to the anti-symmetry of $|u_1\rangle$ and $|u_2\rangle$.

300 Therefore, Eq. (B.8) is now simplified to

$$e = \frac{2}{\pi} \int_{BZ} d^2\mathbf{k} \langle u_1 | [\partial_{k_x} \text{Re}\tilde{P}, \partial_{k_y} \text{Re}\tilde{P}] | u_2 \rangle. \tag{B.20}$$

301 The relevant operator in the above expression is $\text{Re}\tilde{P}$. By introducing the real projector

$$\hat{P} := \sum_n^{\text{occ}} |u_n\rangle \langle u_n|, \tag{B.21}$$

302 we obtain the following identities:

$$\hat{P} = 2\text{Re}\tilde{P} \quad (\text{B.22})$$

303 and

$$\hat{P}|u_n\rangle = |u_n\rangle. \quad (\text{B.23})$$

304 Thus, the formula Eq. (B.20) of the Euler number can be further expressed as:

$$e = \frac{1}{2\pi} \int_{BZ} d^2\mathbf{k} \langle u_1 | \hat{P} [\partial_{k_x} \hat{P}, \partial_{k_y} \hat{P}] | u_2 \rangle. \quad (\text{B.24})$$

305 Due to the symmetry of $k_{x,y}$ and $|u_{1,2}\rangle$, the final form of the Euler number in \mathbf{k} -space is

$$e = \frac{1}{2\pi} \int_{BZ} d^2\mathbf{k} \text{Pf}_{\text{occ}}(\hat{P} [\partial_{k_x} \hat{P}, \partial_{k_y} \hat{P}]), \quad (\text{B.25})$$

306 which is nothing but the Eq. (4) in the main text. Here Pf_{occ} denotes the Pfaffian taken over
307 the occupied subspace. To be specific, in the eigenbasis, a general matrix \mathbf{M} can be represented
308 as a block matrix

$$\mathbf{M} = \begin{pmatrix} M_1 & M_2 \\ M_3 & M_{\text{occ}} \end{pmatrix}, \quad (\text{B.26})$$

309 where M_{occ} is the submatrix of \mathbf{M} constructed by occupied eigenbasis. Therefore, Pf_{occ} , which
310 is the Pfaffian taken over the occupied subspace, is defined as

$$\text{Pf}_{\text{occ}}(M) := \text{Pf}(M_{\text{occ}}). \quad (\text{B.27})$$

311 C Derivation of Eq. (6) in the main text

312 In this section, we derive Eq. (6) in the main text, demonstrating its equivalence to Eq. (4) in
313 the main text under translational invariance.

314 Before proceeding, we first introduce some basic basis for the operators used in the deriva-
315 tion. Firstly, we use a \mathbf{k} -mesh form instead of the continuous form of the system. In real space,
316 the Hamiltonian \hat{H} is constructed under a certain initial local basis $\{|\alpha\mathbf{r}\rangle\}$ with $|\alpha\mathbf{r}\rangle = |\mathbf{r}\rangle \otimes |\alpha\rangle$,
317 i.e.,

$$\hat{H} = \sum_{\alpha'\mathbf{r}', \alpha''\mathbf{r}''} |\alpha'\mathbf{r}'\rangle \langle \alpha''\mathbf{r}'' | H_{\alpha'\mathbf{r}', \alpha''\mathbf{r}''}, \quad (\text{C.1})$$

318 where α and \mathbf{r} denote the internal and coordinate index, respectively. In \mathbf{k} space, it is con-
319 venient to use the Bloch basis $\{|\psi_n(\mathbf{k})\rangle\}$ satisfying $|\psi_n(\mathbf{k})\rangle = |\mathbf{k}\rangle \otimes |u_n(\mathbf{k})\rangle$ where $\{|\mathbf{k}\rangle\}$ is the
320 plane wave basis with $\langle \mathbf{r} | \mathbf{k} \rangle = \frac{1}{\sqrt{A}} e^{-i\mathbf{k}\cdot\mathbf{r}}$ and $A = L_x L_y$ being the area of the system. We can
321 thus construct the \mathbf{k} -space Hamiltonian $\hat{H}(\mathbf{k})$ as

$$\begin{aligned} \hat{H}(\mathbf{k}) &= \langle \mathbf{k} | \hat{H} | \mathbf{k} \rangle \\ &= \sum_{\alpha', \alpha''} |\alpha'(\mathbf{k})\rangle \langle \alpha''(\mathbf{k}) | H_{\alpha', \alpha''}(\mathbf{k}) \\ &= \sum_n |u_n(\mathbf{k})\rangle \langle u_n(\mathbf{k}) | E_n(\mathbf{k}). \end{aligned} \quad (\text{C.2})$$

322 Here, the second equality is established due to the translational invariance of the Hamiltonian.
323 Additionally, the cell-periodic Bloch basis $\{|u_n(\mathbf{k})\rangle\}$ is the eigenbasis of $\hat{H}(\mathbf{k})$.

324 Then, we can define the projection operator acting on different basis sets as [83]

$$\begin{aligned}
\hat{P} &= \sum_{nk}^{\text{occ}} |\psi_n(\mathbf{k})\rangle \langle \psi_n(\mathbf{k})| \\
&= \sum_{\mathbf{k}} |\mathbf{k}\rangle \langle \mathbf{k}| \sum_n^{\text{occ}} |u_n(\mathbf{k})\rangle \langle u_n(\mathbf{k})| \\
&= \sum_{\mathbf{k}} |\mathbf{k}\rangle \langle \mathbf{k}| \sum_{\alpha', \alpha''} |\alpha'(\mathbf{k})\rangle \langle \alpha''(\mathbf{k})| P_{\alpha', \alpha''}(\mathbf{k}) \\
&= \sum_{\mathbf{k}, \alpha', \alpha''} |\alpha' \mathbf{k}\rangle \langle \alpha'' \mathbf{k}| P_{\mathbf{k}, \alpha', \alpha''} \\
&= \sum_{\alpha' \mathbf{r}', \alpha'' \mathbf{r}''} |\alpha' \mathbf{r}'\rangle \langle \alpha'' \mathbf{r}''| P_{\alpha' \mathbf{r}', \alpha'' \mathbf{r}''}.
\end{aligned} \tag{C.3}$$

325 So the \mathbf{k} -space projector $\hat{P}(\mathbf{k}) = \sum_n^{\text{occ}} |u_n(\mathbf{k})\rangle \langle u_n(\mathbf{k})|$ can be explicitly represented as a matrix
326 $P(\mathbf{k})$ under basis $\{|\alpha(\mathbf{k})\rangle\}$. For convenience, we can create a new projection matrix $P_{\mathbf{k}}$, which
327 is a quasi-diagonal matrix with $P(\mathbf{k})$ as diagonal blocks. In fact, $P_{\mathbf{k}}$ represents \hat{P} under basis
328 set $\{|\alpha \mathbf{k}\rangle\}$ and is related to P under basis set $\{|\alpha \mathbf{r}\rangle\}$ via a unitary basis transformation. Specifi-
329 cally, we can construct a transformation matrix $U_{\mathbf{k}, \mathbf{r}}$ with the entries as $\langle \mathbf{r} | \mathbf{k} \rangle$ to denote this
330 basis transformation. Notice that $U_{\mathbf{k}, \mathbf{r}}$ is indeed a unitary matrix in the thermodynamic limit
331 $A \rightarrow \infty$. Therefore, we can obtain the \mathbf{r} -space projection matrix P under the local basis by
332 transforming $P_{\mathbf{k}}$ using the the transformation:

$$P_{\mathbf{k}} = U_{\mathbf{k}, \mathbf{r}} P U_{\mathbf{k}, \mathbf{r}}^\dagger. \tag{C.4}$$

333 Now we start to derive Eq. (6). Since the integral is now discretized as

$$\frac{A}{(2\pi)^2} \int_{BZ} d^2 \mathbf{k} \rightarrow \sum_{\mathbf{k}}, \tag{C.5}$$

334 we can define its equivalent operation $\text{Tr}_{\mathbf{k}}$ acting on the block index \mathbf{k} of $P_{\mathbf{k}}$. Therefore, the
335 \mathbf{k} -space Euler number can be expressed in the matrix form as

$$e = \frac{2\pi}{A} \text{Tr}_{\mathbf{k}} \text{Pf}_{\text{occ}}(P_{\mathbf{k}} [\partial_{k_x} P_{\mathbf{k}}, \partial_{k_y} P_{\mathbf{k}}]). \tag{C.6}$$

336 In a translational invariant system, the \mathbf{k} space and the coordinate space can be connected
337 via the Fourier transformation. Therefore, we have

$$\begin{aligned}
\partial_{k_x} \hat{P}(\mathbf{k}) &\rightarrow \frac{1}{\delta k_x} (P_{\mathbf{k}+\delta \mathbf{k}} - P_{\mathbf{k}}) \\
&= \frac{1}{\delta k_x} (U_{\mathbf{k}+\delta \mathbf{k}, \mathbf{r}} P U_{\mathbf{k}+\delta \mathbf{k}, \mathbf{r}}^\dagger - U_{\mathbf{k}, \mathbf{r}} P U_{\mathbf{k}, \mathbf{r}}^\dagger) \\
&= U_{\mathbf{k}, \mathbf{r}} \left[\frac{1}{\delta k_x} (U_{\delta \mathbf{k}, \mathbf{r}} P U_{\delta \mathbf{k}, \mathbf{r}}^\dagger - P) \right] U_{\mathbf{k}, \mathbf{r}}^\dagger,
\end{aligned} \tag{C.7}$$

338 where $\delta \mathbf{k} = (\delta k_x, 0)$. If we set $\delta k_x = \frac{2\pi}{L_x}$, then $U_{\delta \mathbf{k}, \mathbf{r}}$ is just the unitary position matrix
339 $U = e^{i \frac{2\pi}{L_x} X}$. Similarly, the relation applies to the other unitary position matrix $V = e^{i \frac{2\pi}{L_y} Y}$.

340 Based on these quantities defined in \mathbf{r} space, the Euler number in Eq. (C.6) can be refor-
341 mulated as

$$\begin{aligned}
e &= \frac{1}{2\pi} \text{Pf}_{\text{occ}} \sum_{\mathbf{k}} U_{\mathbf{k}, \mathbf{r}} P [U P U^\dagger, V P V^\dagger] U_{\mathbf{k}, \mathbf{r}}^\dagger \\
&= \frac{1}{2\pi} \text{Pf}_{\text{occ}} \text{Tr}(U_{\mathbf{k}, \mathbf{r}} P [U P U^\dagger, V P V^\dagger] U_{\mathbf{k}, \mathbf{r}}^\dagger) \\
&= \frac{1}{2\pi} \text{Pf}_{\text{occ}} \text{Tr}(P [U P U^\dagger, V P V^\dagger]),
\end{aligned} \tag{C.8}$$

342 where the last equation holds because of the invariant property of the trace under any unitary
 343 transformation. Since the trace and Pfaffian operations act on different individual subspaces,
 344 they are commutative as operators on the Wannier basis with $N_{\text{occ}} = 2$, which proves exactly
 345 the Eq. (6).

346 In principle, when δ_{k_x} is small enough, one can perform the Taylor expansion up to the
 347 first order

$$\frac{1}{\delta k_x} (U_{\delta \mathbf{k}, r} P U_{\delta \mathbf{k}, r}^\dagger - P) \approx i[X, P] \quad (\text{C.9})$$

348 to the right side of Eq. (C.7). However, for a \mathcal{PT} -symmetric system with real eigenbasis
 349 $\{|u_n(\mathbf{k})\}$, both the projection operator P_k and its derivative $\partial_{k_x} P_k$ are supposed to be real-
 350 valued. The first-order expansion term $i[X, P]$, which deviates from the real field \mathbb{R} , should
 351 cancel with some other first-order terms (and higher-order terms may contribute significantly)
 352 to ensure the real-valued final expression. Therefore, the additional real-value limitation from
 353 the \mathcal{PT} symmetry necessitates the use of the unitary position matrix U instead of the usual
 354 position matrix X in our final expression of the r -space Euler number. This is different from
 355 the case of the Chern number where the first-order expansion is applicable to yield a simplified
 356 r -space formula in Ref. [11, 14].

357 D Numerical implementation of the real-space Euler number

358 In this section, we demonstrate the practical calculation of Eq. (6) in the main text. We begin
 359 by selecting a suitable basis for expressing the operators in the equation. Once this basis is
 360 established, we can straightforwardly apply trace and Pfaffian operations.

361 We initially work with a set of local coordinate space bases, from which we construct
 362 diagonal matrices representing the unitary position operators \hat{U} and \hat{V} . The projector \hat{P} is
 363 defined as

$$\mathbf{1}_{\text{occ}} = \begin{pmatrix} \mathbf{0} & \mathbf{0} \\ \mathbf{0} & \mathbf{1} \end{pmatrix} \quad (\text{D.1})$$

364 in the eigenbasis of the Hamiltonian, with eigenvalues arranged in descending order. Here, $\mathbf{0}$
 365 and $\mathbf{1}$ represent the null matrix and identity matrix, respectively.

366 To proceed, we diagonalize the Hamiltonian to obtain the eigenvalues and eigenvectors in
 367 the local basis. This allows us to create a unitary transformation matrix from the local basis to
 368 the eigenbasis of the system. In other words, we have

$$H = \Pi D \Pi^{-1}, \quad (\text{D.2})$$

369 where D is a diagonal matrix with the eigenvalues in descending order, and the columns of Π
 370 are the corresponding eigenvectors. Subsequently, we determine the explicit expression of the
 371 projector \hat{P} through this unitary transformation of the basis, as follows:

$$P = \Pi \mathbf{1}_{\text{occ}} \Pi^{-1}. \quad (\text{D.3})$$

372 All operators are now represented in a unified local basis, simplifying the matrix calcula-
 373 tions. To carry out the trace and Pfaffian operations, a basis transformation from the initial lo-
 374 cal basis to a composite Wannier basis is required. This Wannier basis can be constructed from
 375 the eigenbasis by minimizing the Marzari-Vanderbilt localization functional [82, 83]. Once we
 376 have the transformation matrix Π from the eigenbasis to the local basis and S from the eigen-
 377 basis to the composite Wannier basis, we can obtain the matrix form of the expression within
 378 the brackets in Eq. (C.8):

$$M = S \Pi^{-1} P [U P U^\dagger, V P V^\dagger] \Pi S^{-1}. \quad (\text{D.4})$$

379 In this basis, the matrix entries are denoted as $M_{n'n'',r'r''}$. Then the trace operation simply
 380 involves summing over the coordinate index r , expressed as

$$\text{Tr} := \sum_{r',r''} \delta_{r',r''}. \quad (\text{D.5})$$

381 Finally, the r -space Euler number can be obtained by performing the Pfaffian over occupied
 382 space as ¹

$$\text{Pf}_{\text{occ}}(\text{Tr}M) = \text{Pf}(\text{Tr}M)_{\text{occ}}. \quad (\text{D.6})$$

383 The final step of basis transformation is crucial for accurately calculating the r -space Euler
 384 number. This transformation is necessary because only in the Wannier basis can we effec-
 385 tively separate the total space into internal and coordinate spaces. When using a set of local
 386 basis functions with high localization properties, such as atomic orbitals, the hopping terms
 387 of the Hamiltonian naturally mix the coordinate and internal spaces. As a result, it becomes
 388 challenging to distinguish the occupied subspace within the internal space, making it difficult
 389 to perform the Pfaffian operation using this basis. On the other hand, the eigenbasis of the
 390 Hamiltonian is not suitable either. Although it allows for the easy identification of the occupied
 391 subspace, this highly delocalized basis presents difficulties in aligning it in a meaningful way
 392 to perform the trace and Pfaffian operations correctly.

393 E The distinction between the real-space Chern and Euler num- 394 bers

395 In this section, we give some remarks on the distinction between the real-space Chern and
 396 Euler numbers. First, the analysis we've conducted can be directly applied to the Chern class,
 397 and the resultant r -space expression is nothing but the Bott index,

$$\text{Bott}(\hat{U}, \hat{V}) = \frac{1}{2\pi} \text{ImTr} \log(\hat{U}\hat{V}\hat{U}^{-1}\hat{V}^{-1}), \quad (\text{E.1})$$

398 with $\hat{U} = \hat{P} \exp(2\pi i \hat{X}/L_x) \hat{P}$ and $\hat{V} = \hat{P} \exp(2\pi i \hat{Y}/L_y) \hat{P}$, which measures the commutativity
 399 of the position operators and offers an identical topological classification as the Chern number
 400 [14, 15]. The Bott index can be further simplified by applying the Taylor expansion of the
 401 unitary position operator up to the first order, which yields the conventional r -space formula
 402 of the Chern number in Ref. [11, 14]

$$c_1 = \frac{4\pi}{L^2} \text{ImTr}'(\hat{P}[\hat{X}, \hat{P}][\hat{Y}, \hat{P}]), \quad (\text{E.2})$$

403 where \hat{X}, \hat{Y} are the usual position operators and Tr' is the usual trace operation acting on the
 404 whole space, distinguished from the aforementioned Tr acting on coordinate subspace only.

405 However, there are significant differences between the r -space formulation of the Euler
 406 defined in Eq. (6) and Chern number. This distinction arises because the Chern and Euler
 407 classes are defined by distinct invariant polynomials of the curvature [81]. When calculating
 408 the Chern number in real space, the trace operation is applied to both the internal and coordi-
 409 nate spaces, resulting in a simplified expression with only a single trace operation. In contrast,
 410 when calculating the r -space Euler number, it becomes essential to distinguish between the
 411 coordinate space and the internal space, which requires trace and Pfaffian operations, respec-
 412 tively.

¹The package code is available at <https://github.com/li-dexin-phy/realeulernum>.

413 The discussion is more clear in the frame of matrix form. For any operator of the form
 414 $M = \begin{pmatrix} \mathbf{0} & \mathbf{0} \\ \mathbf{0} & M_{occ} \end{pmatrix}$ with $\mathbf{0}$ being the null matrix, the relation $\text{Tr}_{occ} M := \text{Tr} M_{occ} = \text{Tr} \begin{pmatrix} \mathbf{0} & \mathbf{0} \\ \mathbf{0} & M_{occ} \end{pmatrix}$
 415 always holds. This is because the trace operation is just to sum over the diagonal of the matrix
 416 M , which means that the trace over a specific matrix is equal to the trace over the direct sum
 417 of this matrix and any null matrix. Therefore, we can safely consider the whole space without
 418 further restriction in the occupied space and the result remains the same. However, the Pfaffian
 419 does not possess this property, i.e., $\text{Pf} \begin{pmatrix} \mathbf{0} & \mathbf{0} \\ \mathbf{0} & M_{occ} \end{pmatrix} = \mathbf{0}$. What's more, the ordering of the
 420 basis does not matter for the trace since the sum operation is commutative, while the ordering
 421 is crucial in the definition of the Pfaffian. Therefore, although a single Tr' is enough for
 422 calculating the \mathbf{r} -space Chern number, it is important to find such a basis that can distinguish
 423 the internal space from the coordinate space.

424 This distinction is already evident in the \mathbf{k} -space scenario. In a periodic lattice, the Bloch
 425 states $\{|\psi_n(\mathbf{k})\rangle\}$ can be transformed into Wannier states, which inherently distinguish the
 426 coordinate space from the internal space. Specifically, in such a translational invariant system,
 427 the Hamiltonian commutes with the translation operator, indicating a common eigenvalue for
 428 both operators. Since the energy index n and \mathbf{k} denoting quasi-momentum are independent
 429 of each other, it is straightforward to change the basis of \mathbf{k} via the Fourier transformation
 430 to \mathbf{r} without mixture from n and derive the Wannier basis. However, if the system lacks
 431 translational invariance, the usual Fourier transformation from Bloch states fails to generate
 432 Wannier states. Consequently, it becomes crucial to consider composite Wannier functions
 433 defined in real space via a unitary transformation from energy eigenstates, without imposing
 434 further restrictions.

435 Secondly, It is worth noting that there is a gauge freedom in the Wannier functions and the
 436 determination of the exponentially localized Wannier functions is significant [82]. The existence
 437 of the nontrivial Euler number prohibits finding such a basis of Wannier functions, which
 438 means that in a space-time inversion symmetric two-dimensional system, the exponentially localized
 439 Wannier functions can not be constructed in a phase with nontrivial Euler number [49].
 440 Nevertheless, this is not an obstacle to search for the required composite Wannier functions
 441 that are not exponentially localized [86].

442 F Averaging the local Euler marker in finite systems with OBC

443 In finite systems with OBC, a striking contrast emerges between the local Chern marker and the
 444 local Euler marker. While averaging the local Chern marker over such systems yields vanishing
 445 results, the same averaging process for the local Euler marker results in non-vanishing values.
 446 This disparity highlights a fundamental distinction between the Chern number and the Euler
 447 number when calculated in finite systems under OBC, as elaborated below.

448 To calculate the \mathbf{r} -space Chern number c_1 in Eq. (E.2), we employ standard position operators
 449 \hat{X} and \hat{Y} to construct the operator $\hat{P}[\hat{X}, \hat{P}][\hat{Y}, \hat{P}]$. Notably, the imaginary part of this
 450 operator is directly proportional to c_1 when subjected to a trace operation [11, 14]:

$$c_1 \propto \text{ImTr}'(\hat{P}[\hat{X}, \hat{P}][\hat{Y}, \hat{P}]). \quad (\text{E1})$$

451 Utilizing the transpose invariance and the cyclic property of the trace operation and considering
 452 the symmetry of operators \hat{X} and \hat{Y} , we can rigorously demonstrate the vanishing of the

453 r -space Chern number under OBC [14]:

$$\begin{aligned}
c_1 &\propto \text{ImTr}'(\hat{P}[\hat{X}, \hat{P}][\hat{Y}, \hat{P}]) \\
&= \text{ImTr}'(\hat{P}(\hat{X}\hat{P} - \hat{P}\hat{X})(\hat{Y}\hat{P} - \hat{P}\hat{Y})) \\
&= \text{ImTr}'(\hat{P}\hat{X}\hat{P}\hat{Y}\hat{P} - \hat{P}\hat{X}\hat{P}^2\hat{Y} - \hat{P}^2\hat{X}\hat{Y}\hat{P} + \hat{P}^2\hat{X}\hat{P}\hat{Y}) \\
&= \text{ImTr}'(\hat{P}\hat{X}\hat{P}\hat{Y}\hat{P} - \hat{P}\hat{X}\hat{P}\hat{Y} - \hat{P}\hat{X}\hat{Y}\hat{P} + \hat{P}\hat{X}\hat{P}\hat{Y}) \\
&= \text{ImTr}'(\hat{P}\hat{X}\hat{P}\hat{Y}\hat{P} - \hat{P}\hat{X}\hat{Y}\hat{P}), \tag{F2}
\end{aligned}$$

454 where we utilize the property of the projection operator, $\hat{P}^2 = \hat{P}$. Note that \hat{P} , \hat{X} and \hat{Y} are all
455 Hermitian, we can further simplify c_1 by expanding the imaginary part as the subtract of the
456 operator with its conjugate,

$$\begin{aligned}
c_1 &\propto \frac{1}{2i}(\text{Tr}'(\hat{P}\hat{X}\hat{P}\hat{Y}\hat{P} - \hat{P}\hat{X}\hat{Y}\hat{P}) - \text{Tr}'(\hat{P}\hat{X}\hat{P}\hat{Y}\hat{P} - \hat{P}\hat{X}\hat{Y}\hat{P})^*) \\
&= \frac{1}{2i}(\text{Tr}'(\hat{P}\hat{X}\hat{P}\hat{Y}\hat{P} - \hat{P}\hat{X}\hat{Y}\hat{P}) - \text{Tr}'(\hat{P}\hat{X}\hat{P}\hat{Y}\hat{P} - \hat{P}\hat{X}\hat{Y}\hat{P})^\dagger) \\
&= \frac{1}{2i}(\text{Tr}'(\hat{P}\hat{X}\hat{P}\hat{Y}\hat{P} - \hat{P}\hat{X}\hat{Y}\hat{P}) - \text{Tr}'(\hat{P}\hat{Y}\hat{P}\hat{X}\hat{P} - \hat{P}\hat{Y}\hat{X}\hat{P})). \tag{F3}
\end{aligned}$$

457 This relationship is established through the transpose invariance of the trace operation, i.e.,

$$\text{Tr}'\hat{A} = \text{Tr}'\hat{A}^T, \tag{F4}$$

458 which leads to

$$\text{ImTr}'\hat{A} = \frac{1}{2i}(\text{Tr}'\hat{A} - \text{Tr}'\hat{A}^*) = \frac{1}{2i}(\text{Tr}'\hat{A} - \text{Tr}'\hat{A}^\dagger). \tag{F5}$$

459 Then, using the well-known cyclic property of trace operation, i.e., for general matrices \hat{A} and
460 \hat{B} , it is known that

$$\text{Tr}'(\hat{A}\hat{B}) = \text{Tr}'(\hat{B}\hat{A}), \tag{F6}$$

461 c_1 can be further simplified as

$$\begin{aligned}
c_1 &\propto \frac{1}{2i}(\text{Tr}'(\hat{P}\hat{X}\hat{P}\hat{Y}\hat{P}) - \text{Tr}'(\hat{P}\hat{X}\hat{Y}\hat{P}) - \text{Tr}'(\hat{P}\hat{Y}\hat{P}\hat{X}\hat{P}) + \text{Tr}'(\hat{P}\hat{Y}\hat{X}\hat{P})) \\
&= \frac{1}{2i}(\text{Tr}'(\hat{X}\hat{P}\hat{Y}\hat{P}^2) - \text{Tr}'(\hat{X}\hat{P}^2\hat{Y}\hat{P}) - \text{Tr}'(\hat{X}\hat{Y}\hat{P}^2) + \text{Tr}'(\hat{Y}\hat{X}\hat{P}^2)) \\
&= \frac{1}{2i}(\text{Tr}'(\hat{X}\hat{P}\hat{Y}\hat{P}) - \text{Tr}'(\hat{X}\hat{P}\hat{Y}\hat{P}) - \text{Tr}'(\hat{X}\hat{Y}\hat{P}) + \text{Tr}'(\hat{Y}\hat{X}\hat{P})) \\
&= -\frac{1}{2i}\text{Tr}'(\hat{X}\hat{Y}\hat{P} - \hat{Y}\hat{X}\hat{P}) \\
&= -\frac{1}{2i}\text{Tr}'([\hat{X}, \hat{Y}]\hat{P}) \\
&= 0, \tag{F7}
\end{aligned}$$

462 where we have used the the symmetry of operators \hat{X} and \hat{Y}

$$[\hat{X}, \hat{Y}] = 0. \tag{F8}$$

463 In summary, the vanishing of the r -space Chern number under OBC arises from a cancel-
464 lation effect, driven by three key factors:

- 465 • Transpose invariance of the trace operation: $\text{Tr}'\hat{A} = \text{Tr}'\hat{A}^T$.
- 466 • Cyclic property of the trace operation: $\text{Tr}'(\hat{A}\hat{B}) = \text{Tr}'(\hat{B}\hat{A})$.

467 • Symmetry of standard position operators \hat{X} and \hat{Y} : $[\hat{X}, \hat{Y}] = 0$.

468 In contrast, calculating the \mathbf{r} -space Euler number doesn't encounter a similar cancellation
 469 effect, primarily due to the distinct properties of the trace operation and the Pfaffian. First,
 470 the transpose invariance, which holds for the trace operation, does not apply to the Pfaffian.
 471 For a general skew-symmetric matrices \hat{A} , we have

$$\text{Pf}\hat{A}^T = \text{Pf}(-\hat{A}) = \pm \text{Pf}\hat{A}, \quad (\text{F.9})$$

472 with the additional sign depending on N_{occ} . Second, unlike the trace operation, the Pfaffian
 473 lacks the necessary cyclic properties for straightforward cancellation,

$$\text{Pf}(\hat{A}\hat{B}) \neq \text{Pf}(\hat{B}\hat{A}). \quad (\text{F.10})$$

474 To be more specific, we now defined a \mathbf{r} -space quantity ζ with trace operation only as

$$\begin{aligned} \zeta &= \frac{1}{2\pi} \text{Tr}'(\hat{P}[\hat{P}_U, \hat{P}_V]) \\ &= \frac{1}{2\pi} \text{Tr}'(\hat{P}\hat{P}_U\hat{P}_V - \hat{P}\hat{P}_V\hat{P}_U) \end{aligned} \quad (\text{F.11})$$

475 where $\hat{P}_U = \hat{U}\hat{P}\hat{U}^\dagger$ and $\hat{P}_V = \hat{V}\hat{P}\hat{V}^\dagger$ are defined analogous to the expression of \mathbf{r} -space Euler
 476 number.

477 Since the projector \hat{P} is Hermitian and \hat{U}/\hat{V} are both unitary operators, it is easy to prove
 478 that both operators are Hermitian operators. In addition, we further express the unitary posi-
 479 tion operators \hat{U}^\dagger and \hat{V}^\dagger as

$$\begin{aligned} \hat{U}^\dagger = \hat{U}^{-1} &= \exp(2\pi i(-\hat{X})/L_x) = \hat{I}\hat{U}\hat{I} \\ \text{and } \hat{V}^\dagger = \hat{V}^{-1} &= \exp(2\pi i(-\hat{Y})/L_y) = \hat{I}\hat{V}\hat{I}. \end{aligned} \quad (\text{F.12})$$

480 where \hat{I} is the inversion operator. And in \mathcal{PT} -symmetric system, the projector \hat{P} is invariant
 481 under such inversion.

482 Since both Hamiltonian \hat{H} and projector \hat{P} satisfy the reality condition, the operators share
 483 the transpose invariant property as

$$\begin{aligned} \hat{P}^T &= \hat{P}^{*\dagger} = \hat{P}^\dagger = \hat{P}, \\ \hat{U}^T &= \hat{U}, \\ \hat{V}^T &= \hat{V}, \\ \hat{P}_U^T &= \hat{U}^\dagger \hat{P} \hat{U}, \\ \text{and } \hat{P}_V^T &= \hat{V}^\dagger \hat{P} \hat{V}. \end{aligned} \quad (\text{F.13})$$

484 Now we can obtain the equivalent form of the first term in Eq. (F.11) as

$$\begin{aligned} \frac{1}{2\pi} \text{Tr}'(\hat{P}\hat{P}_U\hat{P}_V) &= \frac{1}{2\pi} \text{Tr}'(\hat{P}\hat{P}_U\hat{P}_V)^T = \frac{1}{2\pi} \text{Tr}'(\hat{P}_V^T \hat{P}_U^T \hat{P}) = \frac{1}{2\pi} \text{Tr}'((\hat{V}\hat{P}\hat{V}^\dagger)^T \hat{P}_U^T \hat{P}) \\ &= \frac{1}{2\pi} \text{Tr}'(\hat{V}^\dagger \hat{P} \hat{V} \hat{P}_U^T \hat{P}) = \frac{1}{2\pi} \text{Tr}'(\hat{I}\hat{V}\hat{I}\hat{P}\hat{I}\hat{V}^\dagger \hat{I}\hat{P}_U^T \hat{I}) = \frac{1}{2\pi} \text{Tr}'(\hat{I}\hat{P}_V \hat{I}\hat{P}_U^T \hat{I}) = \frac{1}{2\pi} \text{Tr}'(\hat{I}\hat{P}_V \hat{P}_U \hat{I}) \\ &= \frac{1}{2\pi} \text{Tr}'(\hat{P}\hat{P}_V\hat{P}_U), \end{aligned} \quad (\text{F.14})$$

485 which is just the second term of Eq. (F.11). Therefore, we prove that ζ is trivial. Again, we
 486 notice that Eq. (F.4) and Eq. (F.5) are used in the first and the last equality respectively.

487 However, in the case of \mathbf{r} -space Euler number e , as we have already discussed via Eq. (F.9)
 488 and Eq. (F.10), such cancellation doesn't exist. Hence, it becomes possible to calculate the
 489 \mathbf{r} -space Euler number under OBC.

490 G Brief discussion of the reality condition in \mathcal{PT} -broken systems

491 Although we focus on the \mathcal{PT} -symmetric system in the main text, it is not a constraint on
 492 calculating the \mathbf{r} -space Euler number. In \mathbf{k} space, since the time reversal \mathcal{T} can be consid-
 493 ered a conjugate operator combined with a unitary matrix and a sign flip of \mathbf{k} , a \mathcal{T} -invariant
 494 Hamiltonian $H(\mathbf{k})$ satisfies $H(\mathbf{k}) = \hat{T}H(\mathbf{k})\hat{T}^{-1} = H^*(-\mathbf{k})$ under a proper basis obtained from
 495 Takagi decomposition. Therefore, only in a few time-reversal invariant momenta with $\mathbf{k} = -\mathbf{k}$
 496 can we derive a real Hamiltonian. To keep the Hamiltonian real in the whole \mathbf{k} -space, an-
 497 other operator such as \mathcal{P} and \mathcal{C}_{2z} that can reverse the sign of \mathbf{k} is essential. However, in \mathbf{r}
 498 space, the time reversal \mathcal{T} no longer acts on the sign of \mathbf{k} . This means that the symmetry
 499 requirement for the reality condition is only the time reversal \mathcal{T} . Therefore, in a finite system
 500 with OBC lacking spatial symmetry, we can again obtain the necessary basis from the initial
 501 local basis via a transformation matrix given by the Takagi decomposition. Under the new
 502 basis, the Hamiltonian is real-valued. By solving the eigenvalue problem of the Hamiltonian
 503 in such basis, the transformation matrix constructed by all eigenfunctions of the Hamiltonian
 504 is real-valued as well. This is just the reality condition necessitated for the definition of the
 505 Euler class. Consequently, one can apply the real-space formula of the Euler number to any
 506 nonmagnetic aperiodic systems with open boundary, such as quasicrystals, and amorphous
 507 materials without any spatial symmetries.

508 H Details of the model and method

509 H.1 Model

510 All the calculations are performed based on the tight-binding Hamiltonian in Eq. (8). The
 511 hopping integral $t_{\mu\nu}(\mathbf{r}_{ij})$ follows the Slater-Koster parameterization which depends on the
 512 orbital type and the directional cosines of the intersite vector $\mathbf{r}_{ij} = \mathbf{r}_i - \mathbf{r}_j$. The hopping
 513 strength is chosen to have an inverse-square decay with the distance as $t_{\mu\nu}(\mathbf{r}_{ij}) \propto |\mathbf{r}_{ij}|^{-2}$. We
 514 adopt the equilibrium interatomic bond length as the unit length a of the systems, which is the
 515 lattice constant for the perfect square lattice and the side length of basic building blocks (square
 516 and rhombus) for the Ammann-Beenker-tiling quasicrystals. In numerical calculations, we set
 517 the unit length of the system $a = 1$ for simplicity.

518 We consider a 2D square lattice with a band inversion at the Γ -point in \mathbf{k} -space between
 519 degenerate $p_{x,y}$ and $d_{x^2-y^2,xy}$ orbitals, as shown in Fig. 1(a). In real space, we investigate
 520 $L \times L$ supercells of the square lattice with periodic boundary condition (PBC) or open boundary
 521 condition (OBC). For convenience, we choose the lattice size L to be an odd integer, which
 522 allows the supercell to possess an inversion center located at its central site.

523 H.2 Disorder of on-site energy

524 The tight-binding Hamiltonian with the onsite disorder is under our consideration as well.
 525 Therefore, we introduce a disorder term to the Hamiltonian H as

$$H(\{\lambda_i\}) = H + \sum_{i\mu} \lambda_i c_{i\mu}^\dagger c_{i\mu}, \quad (\text{H.1})$$

526 where $\{\lambda_i\}$ is a set of random on-site energy added to one-half sites of the whole sample. Here
 527 $\{\lambda_i\}$ distribute uniformly within the interval of $[-W, W]$ with W being the disorder strength.
 528 To preserve the inversion symmetry, the on-site energies of the rest sites of the sample are
 529 determined by inversion. Namely, each pair of sites connected by the inversion symmetry
 530 shares the same on-site energy. The calculations are performed in samples with lattice size

531 $L = 31$. Because of the random character, we average the r -space Euler number over 100
 532 sample configurations for every W . A higher accuracy can be achieved by adopting samples
 533 with larger sizes and doing the statistical average for more samples.

534 H.3 Structural disorder

535 In order to further investigate the applicability of the real-space formula of the Euler number,
 536 we study the effect of in-plane structural disorder in finite samples which lack the translational
 537 periodicity and all other spatial symmetries [99–101]. To illustrate this effect, we assign ran-
 538 dom atomic displacement $\delta = (d \cos \theta, d \sin \theta)$ away from its equilibrium position for each
 539 atom of the aforementioned 2D perfect square lattice, as depicted in Fig. S6(a). Here, θ is
 540 a random azimuth angle uniformly distributed in the interval $[0, 2\pi)$. The amplitude d of
 541 atomic displacements are uniformly distributed in the range $[0, 0.1a)$ with a being the lattice
 542 constant. For the special structural disorder case but preserving the inversion symmetry, one
 543 can assign the random atomic displacement only to the first half of the lattice, and determine
 544 the locations of atoms in the other half of the lattice by the inversion symmetry. As the structure
 545 becomes disordered, the hopping integrals in Eq. (8) also adjust according to local structural
 546 distortions.

547 H.4 Twisted boundary condition for quasicrystals

548 For an octagonal sample of the Ammann-Beenker-tiling quasicrystal, we calculate the energy
 549 spectrum using both OBC and the twisted boundary condition (TBC). To apply TBC, we artifi-
 550 cially glued the opposite edges of an octagonal polygon. Specifically, for an octagonal polygon
 551 with the edge width of L_{edge} , we label the edges as E_p ($p = 1, 2, \dots, 8$) anticlockwise. For the
 552 edge E_p , we define a translation operator, which is perpendicular to the edge and translates
 553 the octagon by a distance of $2L_{edge}$. By applying the translation operator to the finite octag-
 554 onal quasicrystal so that edge E_p of the sample connects with the opposite edge $E_{(p+4) \bmod 8}$
 555 of the translated image sample. Then we consider the hopping cross the edge between site i
 556 in the octagonal sample and site \tilde{j} in the image sample. These extra hoppings also follow the
 557 Slater-Koster parameterization and have inverse-square decay with the distance (i.e., $|r_{i\tilde{j}}|^{-2}$).
 558 Therefore, in addition to the intersite hoppings between sites inside the sample, we also con-
 559 sider extra hoppings between sites near opposite edges. Importantly, by applying TBC, we not
 560 only get rid of the effect of the open boundary but also restore the 8-fold symmetry of the
 561 quasicrystal.

562 H.5 Construction of composite Wannier function

563 The eigenfunctions ϕ_m associated with the energy index m can be obtained by solving the
 564 eigenvalue problem of the Hamiltonian H . Then the required composite Wannier functions
 565 W_n are constructed from ϕ_m as

$$W_n = \sum_m S_{nm} \phi_m, \quad (\text{H.2})$$

566 via the unitary transformation S that can be considered as the combination of a phase term
 567 and a band matrix [91], which can be numerically obtained by minimizing the Wannier spread
 568 functional

$$\Omega = \sum_n [\langle W_n | r^2 | W_n \rangle - \langle W_n | r | W_n \rangle^2]. \quad (\text{H.3})$$

569 Once the Wannier functions are constructed, the internal and coordinate spaces can be eas-
 570 ily separated and the real-space Euler number can be calculated straightforwardly using the
 571 formula given in Eq. (6).

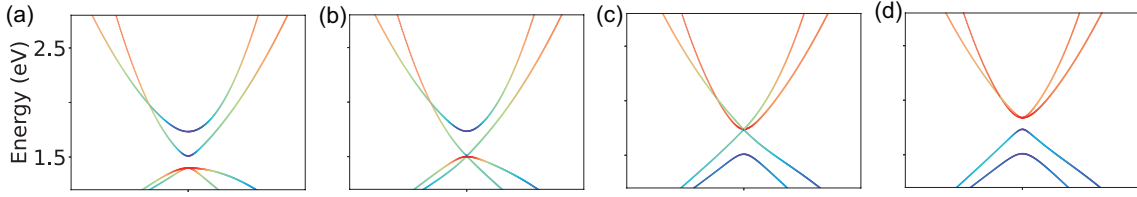


Figure S1: The evolution of band structure around the phase transition in Fig. 1(b). Orbital-resolved band structures near Γ point for the square lattice based on Eq. (8) with different on-site energy difference Δ . (a) $\Delta = 6.76$ eV (region I, $e = 1$). (b) $\Delta = \Delta_1 = 6.86$ eV (the critical point between region I and II). (c) $\Delta = \Delta_2 = 7.10$ eV (the critical point between region II and III). (d) $\Delta = 7.20$ eV (region III, $e = 0$).

572 H.6 Numerical calculation of the k -space Euler number

573 Generally speaking, non-accidental degenerate points (nodes) between the nontrivial occupied
 574 bands are common in k -space [47]. To numerically calculate the k -space Euler number in this
 575 context, we employ the following expression:

$$|e| = \int_{\mathcal{D}} e(\mathcal{F}) - \int_{\partial\mathcal{D}} \langle u_1 | \nabla | u_2 \rangle \cdot \frac{d\mathbf{k}}{2\pi}, \quad (\text{H.4})$$

576 where $e(\mathcal{F}) = (1/\pi) \langle \partial_{k_x} u_1(\mathbf{k}) | \partial_{k_y} u_2(\mathbf{k}) \rangle dk_x \wedge dk_y$, and \mathcal{D} represents the region in the Brill-
 577 ouin zone (BZ) containing those nodes.

578 I More numerical results

579 I.1 Band structures around the topological phase transition in Fig. 1(b)

580 Here we discuss three regions presented in Fig. 1(b) in the main text in detail. These regions
 581 are divided by two critical points $\Delta_1 = 6.86$ and $\Delta_2 = 7.10$ eV. As illustrated in Fig. S1(a), there
 582 is initially a double band inversions occurring around Γ point with $\Delta < \Delta_1$, which accounts
 583 for the nontrivial band topology with $|e| = 1$. This is consistent with the calculations of the
 584 r -space Euler number in the main text, demonstrating that the phase in region I is indeed the
 585 Euler insulator.

586 As the onsite difference Δ increases, the gap decreases gradually and eventually closes at
 587 Δ_1 , as shown in Fig. S1(b). The closing of the gap indicates a topological phase transition.
 588 However, unlike the usual situation of a single band inversion where the gap reopens immedi-
 589 ately after closure accompanied by a sharp change in the topological invariant, our model has
 590 an intermediate gapless region before the gap reopens at Δ_2 as shown in Fig. S1(c). From the
 591 perspective of the band topology, region II is a one-band-inverted phase without protection
 592 from the Euler topology, which accounts for the continuous decreasing of the r -space Euler
 593 number in region II [see Fig. 1(b) in the main text]. In addition, the distinction between the
 594 k -space and r -space Euler number in region II is also due to the closed gap that brings up
 595 the discrimination between \hat{P} projected and the well-defined occupied states. When $\Delta > \Delta_2$
 596 as shown in Fig. S1(d), the gap reopens and there is no band inversion at Γ point anymore.
 597 This phase can be adiabatically connected to the atomic limit without gap closure. Therefore,
 598 region III is a trivial insulator with $e = 0$ as expected.

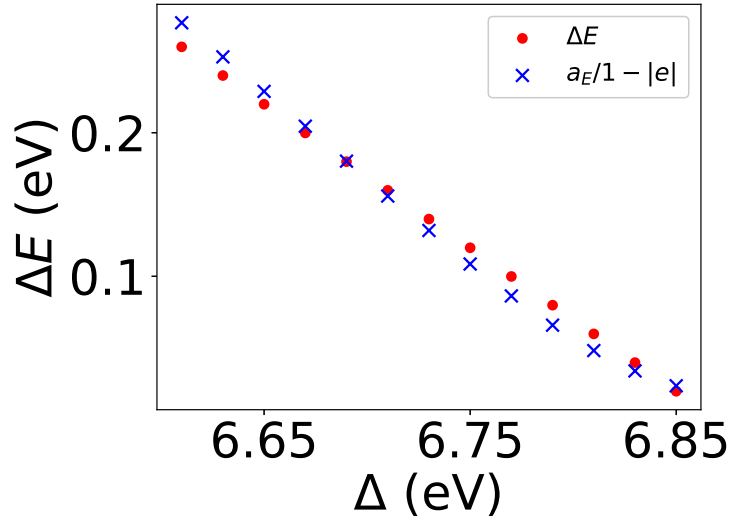


Figure S2: The on-site energy difference Δ dependence of ΔE and $1 - |e|$ with $a_E = 3.125$ meV.

599 I.2 Convergence of the real-space Euler number with decreasing band gap

600 There is a numerical deviation of both k -space and r -space Euler number from an exact integer in regions I and III near the critical points in Fig. 1(b). Here we examine the numerical
601 deviation in region I. As presented in the main text, the r -space Euler number equals the exact
602 one within a correction of order $\mathcal{O}(1/(L\Delta E))$ for systems with lattice size L and energy gap
603 ΔE . For a system with fixed lattice size L , the numerical correction is inversely proportional to
604 the band gap: $1 - |e| \propto 1/\Delta E$, where e is the r -space Euler number. To examine the conver-
605 gence of our r -space formulation as a function of on-site energy difference Δ , we calculate the
606 band gap ΔE and the r -space Euler number in region I for a sample with fixed L . As shown
607 in Fig. S2, we plot the Δ dependence of both ΔE and $a_E/1 - |e|$, where $a_E = 3.125$ meV is a
608 fitting parameter. The inverse of the numerical correction fits well with ΔE as expected, indi-
609 cating that the numerical correction becomes significant near the critical point of the phase
610 transition. Nevertheless, such numerical correction can be diminished by increasing the lattice
611 size.
612

613 I.3 Convergence of the real-space Euler number with increasing lattice size

614 To examine the convergence of real-space Euler number as a function of lattice size L , we
615 further calculate larger systems with the size L up to 90. We consider the pristine lattice with
616 PBC or OBC and a disordered lattice with $W = 1.0$ eV. For the disordered case, we perform
617 an average of the r -space Euler number over 10 samples for each L . As shown in Fig. S3, the
618 curve of the disordered case has not saturated yet but converges slowly towards the quantized
619 value of 1. To further check the convergent behavior, we perform a fitting (see the fitting line
620 in Fig. S3) to estimate the lattice size for the real-space Euler number to reach the quantized
621 value with the error less than 1%. It is found that the required lattice sizes are $L \approx 355$ for
622 the pristine OBC case and $L \approx 570$ for the disordered case respectively, which are beyond the
623 memory limit of our computational resource. As a comparison, the same estimation for the
624 pristine PBC case without disorder shows that a much smaller lattice size of $L \approx 63$ is required
625 to reach the same accuracy. This is because the energy gap is $\Delta E = 0.469$ eV in the pristine
626 PBC case, but for the disordered case with $W = 1.0$ eV, the corresponding averaged gap reduces
627 significantly to $\Delta E = 0.0583$ eV, which is one order of magnitude smaller than the former. This

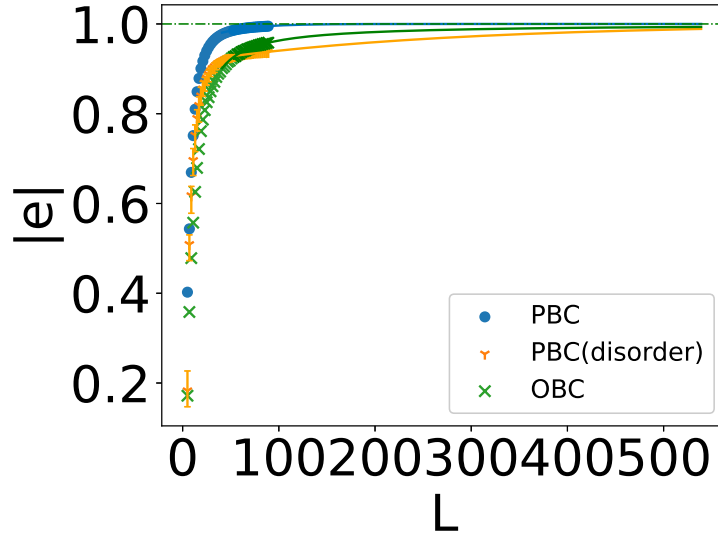


Figure S3: The lattice size L dependence of the \mathbf{r} -space Euler number calculated without and with on-site energy disorder ($W = 1.0$ eV) using PBC, and without disorder using OBC. Fitting curves are added for each case.

628 dependence is illustrated in Fig. S4. As the numeric correction is on the order of $\mathcal{O}(1/(L\Delta E))$
 629 for systems with lattice size L and energy gap ΔE , the much slower convergence rate of the
 630 disordered case is mainly due to the significant reduction of the energy gap reduction in the
 631 presence of disorder.

632 I.4 Local Euler markers in lattices with on-site disorder in Fig. 1(c)

633 In Fig. 1(c) in the main text, we illustrate another intriguing type of topological phase transi-
 634 tion induced by on-site disorder. The averaged \mathbf{r} -space Euler number e decreases from 1 to 0
 635 with increasing the disorder strength W . Here we present the spatial distribution of the local
 636 Euler marker of the sample with PBC at different disorder strengths W , as shown in Fig. S5. At
 637 a relatively weak disorder of $W = 1.2$ eV, the system maintains its nontrivial Euler characteris-
 638 tics. Predominantly, the grid points exhibit nontrivial local Euler markers $e(\mathbf{r}) \approx 1$ with a few
 639 isolated points having vanished $e(\mathbf{r}) \approx 0$, as shown in Fig. S5(a). However, by increasing the
 640 disorder strength W , a noteworthy transformation occurs: the number of trivial points with
 641 $e(\mathbf{r}) \approx 0$ increases, and the trivial area enlarges in size, eventually leaving the nontrivial area
 642 shrinks to an isolated region in the sample [see Fig. S5(c)]. This isolated nontrivial region
 643 with $e(\mathbf{r}) \approx 1$ diminishes in size gradually as W continues to increase, ultimately fragmenting
 644 into small segments [see Fig. S5(d,e)]. Upon reaching $W \geq 2.2$ eV, the situation undergoes a
 645 significant shift. As shown in Fig. S5(f), none of the grid points exhibits nontrivial local Euler
 646 markers, indicating that the system is driven into a trivial phase by strong on-site disorder.
 647 Notably, this type of topological phase transition differs from those in disordered Chern insu-
 648 lators and quantum spin Hall insulators, where a sudden jump of topological invariants occurs
 649 at the critical point [25]. Instead, the disorder-induced transition in this model manifests as
 650 a more continuous evolution. Physically, we conjecture this to be due to the disorder-induced
 651 renormalization of the parameter Δ which dominates the transition from the Euler insulator
 652 to the trivial phase through the intermediate gapless phase, as depicted in Fig. 1(b).

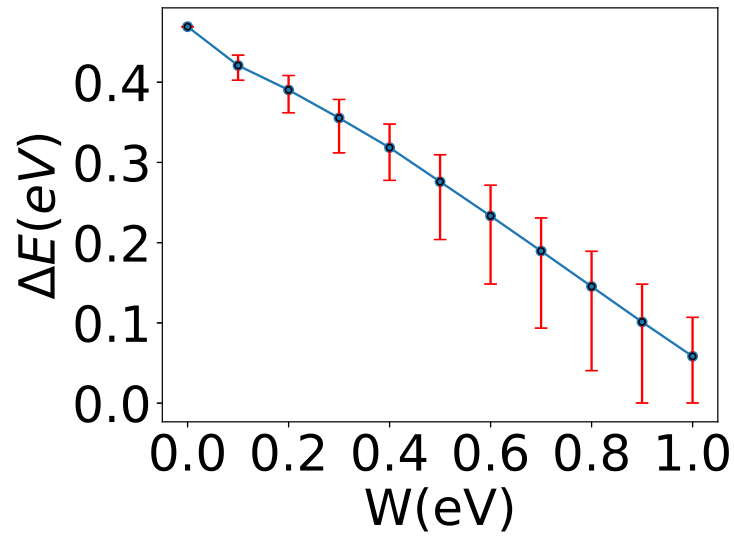


Figure S4: The energy gap ΔE versus on-site energy disorder strength W . For each W , the configuration average is performed over 100 realizations of 51×51 disordered lattices with PBC.

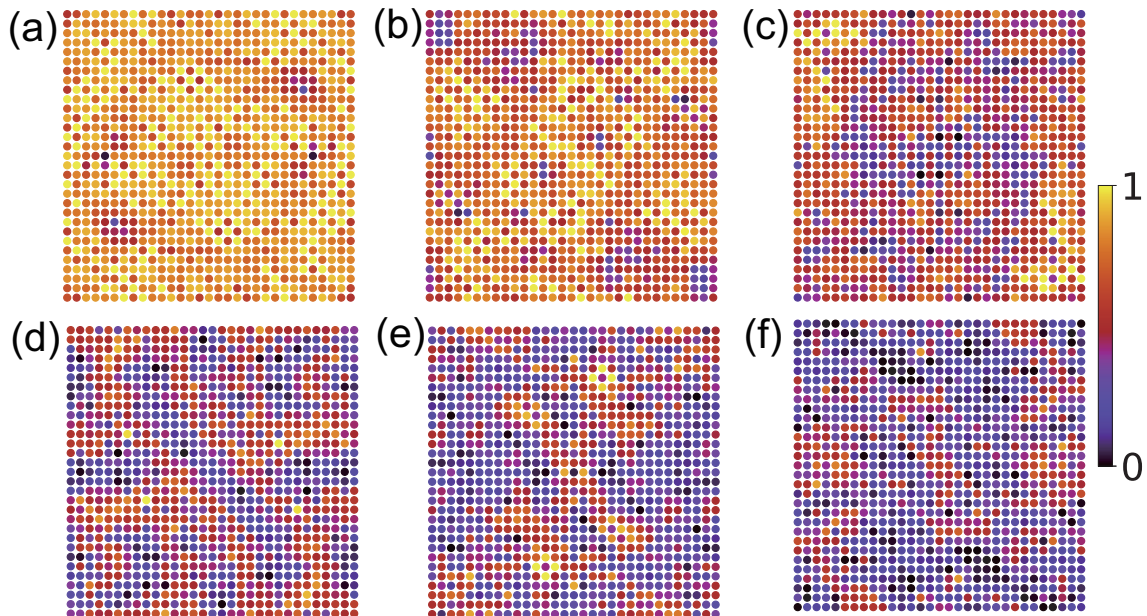


Figure S5: The real-space distribution of local Euler markers $e(\mathbf{r})$ in 31×31 square lattices with PBC at different disorder strength W . (a) $W = 1.2$ eV. (b) $W = 1.4$ eV. (c) $W = 1.6$ eV. (d) $W = 1.8$ eV. (e) $W = 2.0$ eV. (f) $W = 2.2$ eV.

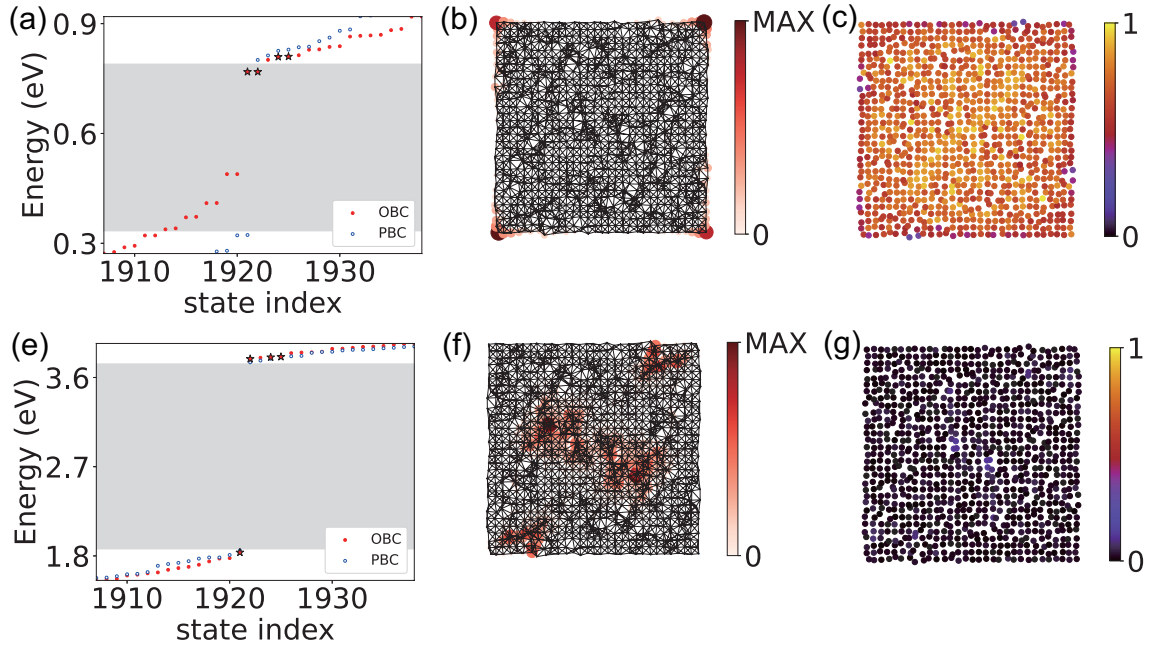


Figure S6: The disordered square lattice model that exhibits band inversions between the (p_x, p_y) and $(d_{x^2-y^2}, d_{xy})$ orbitals. The relevant parameters are as follows: $L = 31$, $\epsilon_{p_x, p_y} = 1.58$, $\epsilon_{d_{x^2-y^2}, d_{xy}} = -0.42$, $V_{pp\sigma} = -0.565$, $V_{pp\pi} = -0.044$, $V_{pd\sigma} = 0.773$, $V_{pd\pi} = 0.335$, $V_{dd\sigma} = 0.444$, $V_{dd\pi} = 0.224$, $V_{dd\delta} = 0.659$ eV. (a) The energy eigenvalues versus the state index in the vicinity of the Fermi level for the disordered square lattice with PBC and OBC. (b) The spatial distribution of the corner states [red stars in (a)]. (c) The real-space distribution of the local Euler marker $e(\mathbf{r})$ for the disordered system with OBC. (e-g) Corresponding results as (a-c) for a trivial state with $e = 0$ (The onsite energy difference is set to $\Delta = 6$ eV).

653 I.5 Euler insulator in lattice with moderate structural disorder

654 In this section, we study the Euler topology of a square lattice with moderate structural dis-
 655 order. We specifically preserve the inversion symmetry at this stage, for comparison with
 656 the case breaking all spatial symmetries presented in Fig. 2 of the main text. To construct
 657 the structurally disordered square lattice [34, 35, 78, 99–101], we add random displacement
 658 $\delta = d(\cos \theta, \sin \theta)$ away from its equilibrium position for each site in one-half sample ($\tau_{1/2}$)
 659 of the square lattice, and assign the displacements for the other half to preserve inversion
 660 symmetry. Here θ and d are determined by uniform distributions in the interval $[0, \pi)$ and
 661 Gaussian distributions with standard deviation $\sigma = 0.2$, respectively. As shown in Fig. S6(a),
 662 the energy spectrum of the structurally disordered lattice with OBC exhibits 4 states at the
 663 Fermi level in the bulk gap obtained using PBC (grey area). We plot the spatial distribution of
 664 these states and find that they are well localized at 4 corners of the sample [see Fig. S6(b)],
 665 implying its higher-order topological feature. Because of the effect of the structural disorder,
 666 the corner states move upwards to the bottom of the unoccupied bulk states. Furthermore, we
 667 analyze the distribution of the local Euler marker in the finite sample with structural disorder,
 668 as shown in Fig. S6(c). The plot confirms that the local Euler markers $e(\mathbf{r})$ are close to the
 669 expected value of 1 in the bulk of the sample, while they deviate in the boundary region. As
 670 expected, the sum of $e(\mathbf{r})$ over the whole finite sample does not vanish but yields the desired
 671 Euler number which should converge to the quantized value with increasing lattice size. Con-
 672 sequently, we can obtain an accurate \mathbf{r} -space Euler number by averaging $e(\mathbf{r})$ over an internal
 673 region of the sample to get rid of the boundary deviation. As a comparison, we also perform
 674 a similar calculation for a trivial phase (see the bottom panels in Fig. S6). As illustrated in
 675 Fig. S6(g), the local Euler marker is almost 0 all over the sample, unambiguously indicating
 676 the trivial nature of the state.

677 I.6 Validation in other models with different Euler numbers

678 In the main text, we present the results based on the tight-binding model with the Euler num-
 679 ber $e = 1$. Now we show that our proposed \mathbf{r} -space formula of the Euler number also applies
 680 to other models with different Euler numbers as well. Different from the tight-binding Hamil-
 681 tonian in Eq. (8) based on the atomic orbital basis, we consider a generic \mathcal{PT} -symmetric
 682 four-band Bloch Hamiltonian $H^{(\chi_1, \chi_2)}(\mathbf{k})$ with (χ_1, χ_2) representing the Euler number of the
 683 upper and lower two-band subspace respectively [97].

684 Specifically, we take $(\chi_1, \chi_2) = (2, 2)$ as an example. The time-reversal \hat{T} and inversion \hat{P}
 685 operators can be expressed as

$$\begin{aligned}\hat{T} &= -i\Gamma_{22}\hat{K}, \\ \hat{P} &= i\Gamma_{22},\end{aligned}\tag{I.1}$$

686 where $\Gamma_{i,j} = \sigma_i \otimes \sigma_j$ are 4×4 Dirac matrices and \hat{K} is the complex conjugation. The minimal
 687 four-band Hamiltonian $H^{(2,2)}(\mathbf{k})$ can be expressed as

$$H^{(2,2)}(\mathbf{k}) = \sin k_1 \Gamma_{01} + \sin k_2 \Gamma_{03} - \left[\frac{1}{2} + \frac{1}{2}(\cos k_1 + \cos k_2) + \frac{3}{2} \cos(k_1 + k_2) \Gamma_{22} + \frac{1}{2} \Gamma_{13} \right].\tag{I.2}$$

688 To calculate the \mathbf{r} -space Euler number in a finite $L \times L$ supercell of the square lattice, we
 689 construct the real-space Hamiltonian $H^{(2,2)}$ by performing the Fourier transformation to the
 690 Bloch Hamiltonian $H^{\chi_1, \chi_2}(\mathbf{k})$, which yields

$$H^{(\chi_1, \chi_2)} = \sum_{ij} \sum_{\mu\nu} \sum_{\mathbf{k} \in \text{BZ}} e^{i\mathbf{k} \cdot (\mathbf{r}_i - \mathbf{r}_j)} [H^{(\chi_1, \chi_2)}(\mathbf{k})]_{\mu\nu} c_{i\mu}^\dagger c_{j\nu}.\tag{I.3}$$

691 Here, \mathbf{r}_i is the lattice vector of the i -th site in the square lattice, and $c_{i\mu}^\dagger$ ($c_{i\mu}$) is electron creation
 692 (annihilation) operator on the μ orbital at the i -th site. For simplicity, we only consider nearest-
 693 neighbor pairs $\langle ij \rangle$ in the lattice. The hopping between site i and j is determined by the
 694 summation over \mathbf{k} in the BZ, $t_{\mu\nu}(\mathbf{r}_{ij}) = \sum_{\mathbf{k} \in \text{BZ}} e^{i\mathbf{k} \cdot (\mathbf{r}_i - \mathbf{r}_j)} [H^{\chi_1, \chi_2}(\mathbf{k})]_{\mu\nu}$. The on-site energies
 695 are given by $\epsilon_\mu = t_{\mu\mu}(\mathbf{0})$.

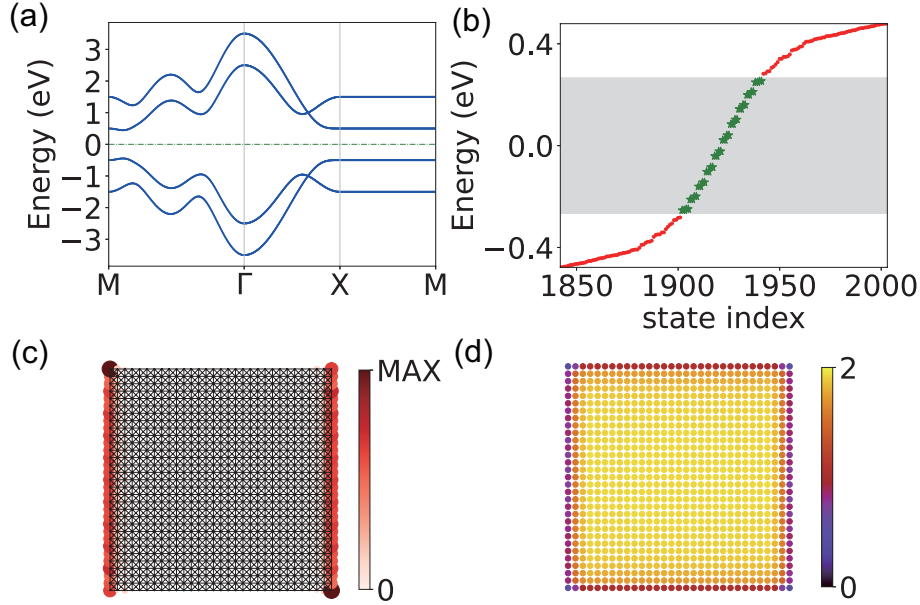


Figure S7: The topological Euler phase with $(\chi_1, \chi_2) = (2, 2)$ in a square lattice based on the minimal four-band model in Eq. (I.3). (a) Band structures of the four-band model in the square lattice. (b) Energy spectrum of a finite sample with OBC. The lattice size is $L = 31$. The bulk gap obtained using PBC is marked in grey. (c) Real-space distribution of the in-gap states [highlighted by green stars in (b)] which are localized on two opposite edges of the finite sample. (d) The real-space distribution of the local Euler marker $e(\mathbf{r})$ in the sample with OBC.

696 The calculated results are shown in Fig. S7. Similar to the Euler insulator with $e = 1$
 697 presented in the main text, the OBC energy spectrum exhibits some states in the bulk gap.
 698 However, these in-gap states are localized on edges instead of corners of the finite sample [see
 699 Fig. S7(c)]. This indicates distinct topological behaviors from the topological Euler insulator
 700 with $e = 1$. According to the relation between the second Stiefel-Whitney number and the
 701 Euler number $w_2 = e \bmod 2$, the Euler insulator with $e = 1$ is also a Stiefel-Whitney insulator
 702 with $w_2 = 1$ which exhibits higher-order topology with corner states in the presence of ad-
 703 ditional chiral symmetry [49, 102]. In contrast, the Euler phase with $e = 2$ leads to a trivial
 704 second Stiefel-Whitney number $w_2 = 0$. Nevertheless, the system associated with the nonzero
 705 Euler number still has a fragile band topology [50]. As shown in Fig. S7 (d), we plot the real-
 706 space distribution of the local Euler marker, which exhibits similar bulk domination and edge
 707 diminution behavior as those studied in the main text. Remarkably, the local Euler markers
 708 inside the bulk are close to the expected value of 2, which results in the averaged \mathbf{r} -space
 709 Euler number being $e = 2$.

710 We further validate our \mathbf{r} -space Euler number in another four-band model with different
 711 Euler numbers for occupied and unoccupied bands. Specifically, we chose the minimal model

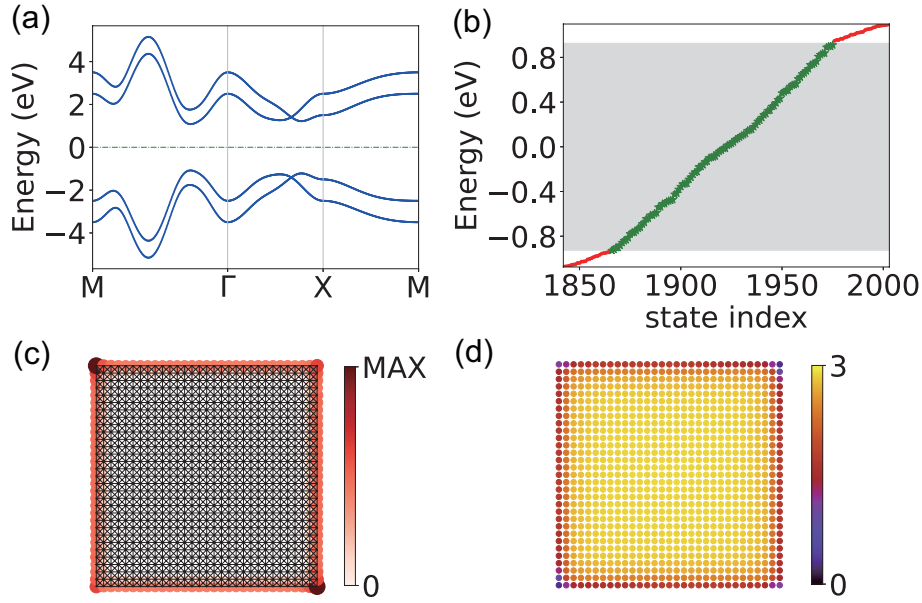


Figure S8: The topological Euler phase with $(\chi_1, \chi_2) = (3, 1)$ in a square lattice based on the minimal four-band model. (a) Band structures of the four-band model in the square lattice. (b) Energy spectrum of a finite sample with OBC. The lattice size is $L = 31$. The bulk gap obtained using PBC is marked in grey. (c) Real-space distribution of the in-gap states [highlighted by green stars in (b)] which are localized on the edges of the finite sample. (d) The real-space distribution of the local Euler marker $e(\mathbf{r})$ in the sample with OBC.

712 with $(\chi_1, \chi_2) = (3, 1)$, which can be formulated as

$$H^{(3,1)}(\mathbf{k}) = \begin{pmatrix} \bar{a} \\ \bar{b} \\ \bar{c} \end{pmatrix}^T \cdot \Gamma \cdot \begin{pmatrix} \bar{a} \\ \bar{b} \\ \bar{c}' \end{pmatrix}, \quad (\text{I.4})$$

713 with

$$\Gamma = \begin{pmatrix} -\Gamma_{33} & -\Gamma_{13} & \Gamma_{01} \\ \Gamma_{31} & \Gamma_{11} & \Gamma_{03} \\ \Gamma_{10} & -\Gamma_{30} & -\Gamma_{22} \end{pmatrix} \quad (\text{I.5})$$

714 and

$$\begin{aligned} \bar{a} &= \sin k_1, \\ \bar{b} &= \sin k_2 \\ \bar{c} &= \frac{1}{2}(1 + (\cos k_1 + \cos k_2) + 3\cos(k_1 + k_2)), \\ \bar{c}' &= \frac{1}{2}(3 - 2(\cos k_1 + \cos k_2) - \cos(k_1 + k_2)). \end{aligned} \quad (\text{I.6})$$

715 The results of the minimal model with $(\chi_1, \chi_2) = (3, 1)$ are illustrated in Fig. S8. In this
 716 case, the unbalanced $|\chi_1| \neq |\chi_2|$ leads to the lack of additional symmetry of the system [103].
 717 Consequently, although the system is a topological phase with nontrivial Stiefel-Whitney num-
 718 ber $w_2 = 1$ because of the odd Euler number of the occupied bands, there is no additional
 719 symmetry to ensure the localization at the corner. Therefore, this phase does not exhibit the
 720 higher-order corner characteristics of conventional Stiefel-Whitney insulators [104–108].

721 **References**

- 722 [1] K. v. Klitzing, G. Dorda and M. Pepper, *New method for high-accuracy determination of*
723 *the fine-structure constant based on quantized Hall resistance*, Phys. Rev. Lett. **45**, 494
724 (1980), doi:[10.1103/PhysRevLett.45.494](https://doi.org/10.1103/PhysRevLett.45.494).
- 725 [2] D. J. Thouless, M. Kohmoto, M. P. Nightingale and M. den Nijs, *Quantized Hall con-*
726 *ductance in a two-dimensional periodic potential*, Phys. Rev. Lett. **49**, 405 (1982),
727 doi:[10.1103/PhysRevLett.49.405](https://doi.org/10.1103/PhysRevLett.49.405).
- 728 [3] M. Kohmoto, *Topological invariant and the quantization of the Hall conductance*, Annals
729 of Physics **160**(2), 343 (1985), doi:[https://doi.org/10.1016/0003-4916\(85\)90148-4](https://doi.org/10.1016/0003-4916(85)90148-4).
- 730 [4] B. I. Halperin, *Quantized Hall conductance, current-carrying edge states, and the exist-*
731 *ence of extended states in a two-dimensional disordered potential*, Phys. Rev. B **25**, 2185
732 (1982), doi:[10.1103/PhysRevB.25.2185](https://doi.org/10.1103/PhysRevB.25.2185).
- 733 [5] Y. Hatsugai, *Chern number and edge states in the integer quantum Hall effect*, Phys. Rev.
734 Lett. **71**, 3697 (1993), doi:[10.1103/PhysRevLett.71.3697](https://doi.org/10.1103/PhysRevLett.71.3697).
- 735 [6] D. Xiao, M.-C. Chang and Q. Niu, *Berry phase effects on electronic properties*, Rev. Mod.
736 Phys. **82**, 1959 (2010), doi:[10.1103/RevModPhys.82.1959](https://doi.org/10.1103/RevModPhys.82.1959).
- 737 [7] M. Z. Hasan and C. L. Kane, *Colloquium: Topological insulators*, Rev. Mod. Phys. **82**,
738 3045 (2010), doi:[10.1103/RevModPhys.82.3045](https://doi.org/10.1103/RevModPhys.82.3045).
- 739 [8] X.-L. Qi and S.-C. Zhang, *Topological insulators and superconductors*, Rev. Mod. Phys.
740 **83**, 1057 (2011), doi:[10.1103/RevModPhys.83.1057](https://doi.org/10.1103/RevModPhys.83.1057).
- 741 [9] T. Fukui, Y. Hatsugai and H. Suzuki, *Chern numbers in discretized Brillouin zone: Efficient*
742 *method of computing (spin) Hall conductances*, J. Phys. Soc. Japan **74**(6), 1674 (2005),
743 doi:[10.1143/JPSJ.74.1674](https://doi.org/10.1143/JPSJ.74.1674).
- 744 [10] A. Kitaev, *Anyons in an exactly solved model and beyond*, Annals of Physics **321**(1), 2
745 (2006), doi:<https://doi.org/10.1016/j.aop.2005.10.005>.
- 746 [11] R. Bianco and R. Resta, *Mapping topological order in coordinate space*, Phys. Rev. B **84**,
747 241106 (2011), doi:[10.1103/PhysRevB.84.241106](https://doi.org/10.1103/PhysRevB.84.241106).
- 748 [12] E. Prodan, *Non-commutative tools for topological insulators*, New Journal of Physics
749 **12**(6), 065003 (2010), doi:[10.1088/1367-2630/12/6/065003](https://doi.org/10.1088/1367-2630/12/6/065003).
- 750 [13] T. A. Loring and M. B. Hastings, *Disordered topological insulators via C^* -algebras*, Euro-
751 physics Letters **92**(6), 67004 (2011), doi:[10.1209/0295-5075/92/67004](https://doi.org/10.1209/0295-5075/92/67004).
- 752 [14] D. Toniolo, *On the Bott index of unitary matrices on a finite torus*, Lett. Math. Phys.
753 **112**(6), 126 (2022), doi:[10.1007/s11005-022-01602-6](https://doi.org/10.1007/s11005-022-01602-6).
- 754 [15] M. B. Hastings and T. A. Loring, *Topological insulators and C^* -algebras:*
755 *Theory and numerical practice*, Annals of Physics **326**(7), 1699 (2011),
756 doi:<https://doi.org/10.1016/j.aop.2010.12.013>.
- 757 [16] T. A. Loring, *K -theory and pseudospectra for topological insulators*, Annals of Physics
758 **356**, 383 (2015), doi:<https://doi.org/10.1016/j.aop.2015.02.031>.

- 759 [17] E. Prodan, *Disordered topological insulators: a non-commutative geometry perspective*, Journal of Physics A: Mathematical and Theoretical **44**(11), 113001 (2011),
760 doi:[10.1088/1751-8113/44/11/113001](https://doi.org/10.1088/1751-8113/44/11/113001).
761
- 762 [18] M. D. Caio, G. Möller, N. R. Cooper and M. J. Bhaseen, *Topological marker currents in Chern insulators*, Nature Physics **15**(3), 257 (2019), doi:[10.1038/s41567-018-0390-7](https://doi.org/10.1038/s41567-018-0390-7).
763
- 764 [19] E. Prodan, T. L. Hughes and B. A. Bernevig, *Entanglement spectrum of a disordered topological Chern insulator*, Phys. Rev. Lett. **105**, 115501 (2010),
765 doi:[10.1103/PhysRevLett.105.115501](https://doi.org/10.1103/PhysRevLett.105.115501).
766
- 767 [20] I. C. Fulga, D. I. Pikulin and T. A. Loring, *Aperiodic weak topological superconductors*,
768 Phys. Rev. Lett. **116**, 257002 (2016), doi:[10.1103/PhysRevLett.116.257002](https://doi.org/10.1103/PhysRevLett.116.257002).
- 769 [21] I. Mondragon-Shem, T. L. Hughes, J. Song and E. Prodan, *Topological criticality in the chiral-symmetric AIII class at strong disorder*, Phys. Rev. Lett. **113**, 046802 (2014),
770 doi:[10.1103/PhysRevLett.113.046802](https://doi.org/10.1103/PhysRevLett.113.046802).
771
- 772 [22] S. Velury, B. Bradlyn and T. L. Hughes, *Topological crystalline phases in a disordered inversion-symmetric chain*, Phys. Rev. B **103**, 024205 (2021),
773 doi:[10.1103/PhysRevB.103.024205](https://doi.org/10.1103/PhysRevB.103.024205).
774
- 775 [23] J. Claes and T. L. Hughes, *Disorder driven phase transitions in weak AIII topological insulators*, Phys. Rev. B **101**, 224201 (2020), doi:[10.1103/PhysRevB.101.224201](https://doi.org/10.1103/PhysRevB.101.224201).
776
- 777 [24] H. Huang and F. Liu, *Quantum spin Hall effect and spin Bott index in a quasicrystal lattice*,
778 Phys. Rev. Lett. **121**, 126401 (2018), doi:[10.1103/PhysRevLett.121.126401](https://doi.org/10.1103/PhysRevLett.121.126401).
- 779 [25] H. Huang and F. Liu, *Theory of spin Bott index for quantum spin Hall states in nonperiodic systems*, Phys. Rev. B **98**, 125130 (2018), doi:[10.1103/PhysRevB.98.125130](https://doi.org/10.1103/PhysRevB.98.125130).
780
- 781 [26] H. Huang, Y.-S. Wu and F. Liu, *Aperiodic topological crystalline insulators*, Phys. Rev. B **101**, 041103 (2020), doi:[10.1103/PhysRevB.101.041103](https://doi.org/10.1103/PhysRevB.101.041103).
782
- 783 [27] H. Huang and F. Liu, *Comparison of quantum spin Hall states in quasicrystals and crystals*,
784 Phys. Rev. B **100**, 085119 (2019), doi:[10.1103/PhysRevB.100.085119](https://doi.org/10.1103/PhysRevB.100.085119).
- 785 [28] A. Agarwala and V. B. Shenoy, *Topological insulators in amorphous systems*, Phys. Rev. Lett. **118**, 236402 (2017), doi:[10.1103/PhysRevLett.118.236402](https://doi.org/10.1103/PhysRevLett.118.236402).
786
- 787 [29] S. Kim, A. Agarwala and D. Chowdhury, *Fractionalization and topology in amorphous electronic solids*, Phys. Rev. Lett. **130**, 026202 (2023),
788 doi:[10.1103/PhysRevLett.130.026202](https://doi.org/10.1103/PhysRevLett.130.026202).
789
- 790 [30] X. S. Wang, A. Brataas and R. E. Troncoso, *Bosonic Bott index and disorder-induced topological transitions of magnons*, Phys. Rev. Lett. **125**, 217202 (2020),
791 doi:[10.1103/PhysRevLett.125.217202](https://doi.org/10.1103/PhysRevLett.125.217202).
792
- 793 [31] P. Titum, N. H. Lindner, M. C. Rechtsman and G. Refael, *Disorder-induced Floquet topological insulators*, Phys. Rev. Lett. **114**, 056801 (2015),
794 doi:[10.1103/PhysRevLett.114.056801](https://doi.org/10.1103/PhysRevLett.114.056801).
795
- 796 [32] D. Toniolo, *Time-dependent topological systems: A study of the Bott index*, Phys. Rev. B **98**, 235425 (2018), doi:[10.1103/PhysRevB.98.235425](https://doi.org/10.1103/PhysRevB.98.235425).
797
- 798 [33] B. Kang, W. Lee and G. Y. Cho, *Many-body invariants for Chern and chiral hinge insulators*, Phys. Rev. Lett. **126**, 016402 (2021), doi:[10.1103/PhysRevLett.126.016402](https://doi.org/10.1103/PhysRevLett.126.016402).
799

- 800 [34] Y.-B. Yang, T. Qin, D.-L. Deng, L.-M. Duan and Y. Xu, *Topological amorphous metals*,
801 Phys. Rev. Lett. **123**, 076401 (2019), doi:[10.1103/PhysRevLett.123.076401](https://doi.org/10.1103/PhysRevLett.123.076401).
- 802 [35] J. D. Hannukainen, M. F. Martínez, J. H. Bardarson and T. K. Kvarning, *Local topological*
803 *markers in odd spatial dimensions and their application to amorphous topological matter*,
804 Phys. Rev. Lett. **129**, 277601 (2022), doi:[10.1103/PhysRevLett.129.277601](https://doi.org/10.1103/PhysRevLett.129.277601).
- 805 [36] W. Chen, *Universal topological marker*, Phys. Rev. B **107**, 045111 (2023),
806 doi:[10.1103/PhysRevB.107.045111](https://doi.org/10.1103/PhysRevB.107.045111).
- 807 [37] J. Sykes and R. Barnett, *Local topological markers in odd dimensions*, Phys. Rev. B **103**,
808 155134 (2021), doi:[10.1103/PhysRevB.103.155134](https://doi.org/10.1103/PhysRevB.103.155134).
- 809 [38] A. A. Markov and A. N. Rubtsov, *Local marker for interacting topological insulators*, Phys.
810 Rev. B **104**, L081105 (2021), doi:[10.1103/PhysRevB.104.L081105](https://doi.org/10.1103/PhysRevB.104.L081105).
- 811 [39] B. Irsigler, J.-H. Zheng and W. Hofstetter, *Microscopic characteristics and tomog-*
812 *raphy scheme of the local Chern marker*, Phys. Rev. A **100**, 023610 (2019),
813 doi:[10.1103/PhysRevA.100.023610](https://doi.org/10.1103/PhysRevA.100.023610).
- 814 [40] I. Mondragon-Shem and T. L. Hughes, *Robust topological invariants of topological crys-*
815 *talline phases in the presence of impurities* (2019), [1906.11847](https://arxiv.org/abs/1906.11847).
- 816 [41] A. G. Grushin and C. Repellin, *Amorphous and polycrystalline routes toward a chiral spin*
817 *liquid*, Phys. Rev. Lett. **130**, 186702 (2023), doi:[10.1103/PhysRevLett.130.186702](https://doi.org/10.1103/PhysRevLett.130.186702).
- 818 [42] Y. X. Zhao, A. P. Schnyder and Z. D. Wang, *Unified theory of PT and CP invariant*
819 *topological metals and nodal superconductors*, Phys. Rev. Lett. **116**, 156402 (2016),
820 doi:[10.1103/PhysRevLett.116.156402](https://doi.org/10.1103/PhysRevLett.116.156402).
- 821 [43] Y. X. Zhao and Y. Lu, *PT -symmetric real Dirac Fermions and semimetals*, Phys. Rev. Lett.
822 **118**, 056401 (2017), doi:[10.1103/PhysRevLett.118.056401](https://doi.org/10.1103/PhysRevLett.118.056401).
- 823 [44] J. Ahn and B.-J. Yang, *Unconventional topological phase transition in two-dimensional*
824 *systems with space-time inversion symmetry*, Phys. Rev. Lett. **118**, 156401 (2017),
825 doi:[10.1103/PhysRevLett.118.156401](https://doi.org/10.1103/PhysRevLett.118.156401).
- 826 [45] J. Ahn, D. Kim, Y. Kim and B.-J. Yang, *Band topology and linking structure of nodal*
827 *line semimetals with Z_2 monopole charges*, Phys. Rev. Lett. **121**, 106403 (2018),
828 doi:[10.1103/PhysRevLett.121.106403](https://doi.org/10.1103/PhysRevLett.121.106403).
- 829 [46] Q. Wu, A. A. Soluyanov and T. Bzdušek, *Non-Abelian band topology in noninteracting*
830 *metals*, Science **365**(6459), 1273 (2019), doi:[10.1126/science.aau8740](https://doi.org/10.1126/science.aau8740).
- 831 [47] A. Bouhon, Q. Wu, R.-J. Slager, H. Weng, O. V. Yazyev and T. Bzdušek, *Non-Abelian*
832 *reciprocal braiding of Weyl points and its manifestation in ZrTe*, Nat. Phys. **16**(11), 1137
833 (2020), doi:[10.1038/s41567-020-0967-9](https://doi.org/10.1038/s41567-020-0967-9).
- 834 [48] J. Ahn and B.-J. Yang, *Symmetry representation approach to topological*
835 *invariants in $C_{2z}T$ -symmetric systems*, Phys. Rev. B **99**, 235125 (2019),
836 doi:[10.1103/PhysRevB.99.235125](https://doi.org/10.1103/PhysRevB.99.235125).
- 837 [49] J. Ahn, S. Park and B.-J. Yang, *Failure of Nielsen-Ninomiya theorem and frag-*
838 *ile topology in two-dimensional systems with space-time inversion symmetry: Applica-*
839 *tion to twisted bilayer graphene at magic angle*, Phys. Rev. X **9**, 021013 (2019),
840 doi:[10.1103/PhysRevX.9.021013](https://doi.org/10.1103/PhysRevX.9.021013).

- 841 [50] J. Ahn, S. Park, D. Kim, Y. Kim and B.-J. Yang, *Stiefel–Whitney classes and topological phases in band theory*, Chin. Phys. B **28**(11), 117101 (2019), doi:[10.1088/1674-1056/ab4d3b](https://doi.org/10.1088/1674-1056/ab4d3b).
- 842
843
- 844 [51] H. C. Po, H. Watanabe and A. Vishwanath, *Fragile topology and Wannier obstructions*, Phys. Rev. Lett. **121**, 126402 (2018), doi:[10.1103/PhysRevLett.121.126402](https://doi.org/10.1103/PhysRevLett.121.126402).
- 845
- 846 [52] F. N. Ünal, A. Bouhon and R.-J. Slager, *Topological Euler class as a dynamical observable in optical lattices*, Phys. Rev. Lett. **125**, 053601 (2020), doi:[10.1103/PhysRevLett.125.053601](https://doi.org/10.1103/PhysRevLett.125.053601).
- 847
848
- 849 [53] Y. Guan, A. Bouhon and O. V. Yazyev, *Landau levels of the Euler class topology*, Phys. Rev. Res. **4**, 023188 (2022), doi:[10.1103/PhysRevResearch.4.023188](https://doi.org/10.1103/PhysRevResearch.4.023188).
- 850
- 851 [54] F. Xie, Z. Song, B. Lian and B. A. Bernevig, *Topology-bounded superfluid weight in twisted bilayer graphene*, Phys. Rev. Lett. **124**, 167002 (2020), doi:[10.1103/PhysRevLett.124.167002](https://doi.org/10.1103/PhysRevLett.124.167002).
- 852
853
- 854 [55] A. Kitaev, *Periodic table for topological insulators and superconductors*, AIP Conf. Proc. **1134**(1), 22 (2009), doi:[10.1063/1.3149495](https://doi.org/10.1063/1.3149495).
- 855
- 856 [56] B. Peng, A. Bouhon, B. Monserrat and R.-J. Slager, *Phonons as a platform for non-Abelian braiding and its manifestation in layered silicates*, Nat. Commun. **13**(1), 423 (2022), doi:[10.1038/s41467-022-28046-9](https://doi.org/10.1038/s41467-022-28046-9).
- 857
858
- 859 [57] B. Jiang, A. Bouhon, Z.-K. Lin, X. Zhou, B. Hou, F. Li, R.-J. Slager and J.-H. Jiang, *Experimental observation of non-Abelian topological acoustic semimetals and their phase transitions*, Nature Physics **17**(11), 1239 (2021), doi:[10.1038/s41567-021-01340-x](https://doi.org/10.1038/s41567-021-01340-x).
- 860
861
- 862 [58] H. Qiu, Q. Zhang, T. Liu, X. Fan, F. Zhang and C. Qiu, *Minimal non-abelian nodal braiding in ideal metamaterials*, Nat. Commun. **14**(1), 1261 (2023), doi:[10.1038/s41467-023-36952-9](https://doi.org/10.1038/s41467-023-36952-9).
- 863
864
- 865 [59] M. Wang, S. Liu, Q. Ma, R.-Y. Zhang, D. Wang, Q. Guo, B. Yang, M. Ke, Z. Liu and C. T. Chan, *Experimental observation of non-Abelian earring nodal links in phononic crystals*, Phys. Rev. Lett. **128**, 246601 (2022), doi:[10.1103/PhysRevLett.128.246601](https://doi.org/10.1103/PhysRevLett.128.246601).
- 866
867
- 868 [60] E. Yang, B. Yang, O. You, H.-C. Chan, P. Mao, Q. Guo, S. Ma, L. Xia, D. Fan, Y. Xiang and S. Zhang, *Observation of non-Abelian nodal links in photonics*, Phys. Rev. Lett. **125**, 033901 (2020), doi:[10.1103/PhysRevLett.125.033901](https://doi.org/10.1103/PhysRevLett.125.033901).
- 869
870
- 871 [61] Q. Guo, T. Jiang, R.-Y. Zhang, L. Zhang, Z.-Q. Zhang, B. Yang, S. Zhang and C. T. Chan, *Experimental observation of non-Abelian topological charges and edge states*, Nature **594**(7862), 195 (2021), doi:[10.1038/s41586-021-03521-3](https://doi.org/10.1038/s41586-021-03521-3).
- 872
873
- 874 [62] D. Wang, B. Yang, M. Wang, R.-Y. Zhang, X. Li, Z. Q. Zhang, S. Zhang and C. T. Chan, *Observation of non-Abelian charged nodes linking nonadjacent gaps*, Phys. Rev. Lett. **129**, 263604 (2022), doi:[10.1103/PhysRevLett.129.263604](https://doi.org/10.1103/PhysRevLett.129.263604).
- 875
876
- 877 [63] D. Wang, Y. Wu, Z. Q. Zhang and C. T. Chan, *Non-Abelian frame charge flow in photonic media*, Phys. Rev. X **13**, 021024 (2023), doi:[10.1103/PhysRevX.13.021024](https://doi.org/10.1103/PhysRevX.13.021024).
- 878
- 879 [64] W. Zhao, Y.-B. Yang, Y. Jiang, Z. Mao, W. Guo, L. Qiu, G. Wang, L. Yao, L. He, Z. Zhou, Y. Xu and L. Duan, *Quantum simulation for topological Euler insulators*, Commun. Phys. **5**(1), 223 (2022), doi:[10.1038/s42005-022-01001-2](https://doi.org/10.1038/s42005-022-01001-2).
- 880
881

- 882 [65] B. Jiang, A. Bouhon, S.-Q. Wu, Z.-L. Kong, Z.-K. Lin, R.-J. Slager and J.-H. Jiang, *Experimental observation of meronic topological acoustic Euler insulators* (2022), [2205.03429](https://arxiv.org/abs/2205.03429).
883
- 884 [66] O. Breach, R.-J. Slager and F. N. Ünal, *Interferometry of non-Abelian band singularities and Euler class topology* (2024), [2401.01928](https://arxiv.org/abs/2401.01928).
885
- 886 [67] W. J. Jankowski, A. S. Morris, A. Bouhon, F. N. Ünal and R.-J. Slager, *Optical manifestations of topological Euler class in electronic materials* (2023), [2311.07545](https://arxiv.org/abs/2311.07545).
887
- 888 [68] C. Fang and L. Fu, *New classes of three-dimensional topological crystalline insulators: Nonsymmorphic and magnetic*, Phys. Rev. B **91**, 161105 (2015),
889 doi:[10.1103/PhysRevB.91.161105](https://doi.org/10.1103/PhysRevB.91.161105).
890
- 891 [69] C. Wang, F. Liu and H. Huang, *Effective model for fractional topological corner modes in quasicrystals*, Phys. Rev. Lett. **129**, 056403 (2022),
892 doi:[10.1103/PhysRevLett.129.056403](https://doi.org/10.1103/PhysRevLett.129.056403).
893
- 894 [70] H. Huang, J. Fan, D. Li and F. Liu, *Generic orbital design of higher-order topological quasicrystalline insulators with odd five-fold rotation symmetry*, Nano Lett. **21**(16), 7056
895 (2021), doi:[10.1021/acs.nanolett.1c02661](https://doi.org/10.1021/acs.nanolett.1c02661).
896
- 897 [71] R. Chen, C.-Z. Chen, J.-H. Gao, B. Zhou and D.-H. Xu, *Higher-order topological insulators in quasicrystals*, Phys. Rev. Lett. **124**, 036803 (2020),
898 doi:[10.1103/PhysRevLett.124.036803](https://doi.org/10.1103/PhysRevLett.124.036803).
899
- 900 [72] D. Varjas, A. Lau, K. Pöyhönen, A. R. Akhmerov, D. I. Pikulin and I. C. Fulga, *Topological phases without crystalline counterparts*, Phys. Rev. Lett. **123**, 196401 (2019),
901 doi:[10.1103/PhysRevLett.123.196401](https://doi.org/10.1103/PhysRevLett.123.196401).
902
- 903 [73] S. Spurrier and N. R. Cooper, *Kane-mele with a twist: Quasicrystalline higher-order topological insulators with fractional mass kinks*, Phys. Rev. Res. **2**, 033071 (2020),
904 doi:[10.1103/PhysRevResearch.2.033071](https://doi.org/10.1103/PhysRevResearch.2.033071).
905
- 906 [74] D. V. Else, S.-J. Huang, A. Prem and A. Gromov, *Quantum many-body topology of quasicrystals*, Phys. Rev. X **11**, 041051 (2021), doi:[10.1103/PhysRevX.11.041051](https://doi.org/10.1103/PhysRevX.11.041051).
907
- 908 [75] C.-A. Li, B. Fu, Z.-A. Hu, J. Li and S.-Q. Shen, *Topological phase transitions in disordered electric quadrupole insulators*, Phys. Rev. Lett. **125**, 166801 (2020),
909 doi:[10.1103/PhysRevLett.125.166801](https://doi.org/10.1103/PhysRevLett.125.166801).
910
- 911 [76] W. A. Benalcazar and A. Cerjan, *Chiral-symmetric higher-order topological phases of matter*, Phys. Rev. Lett. **128**, 127601 (2022), doi:[10.1103/PhysRevLett.128.127601](https://doi.org/10.1103/PhysRevLett.128.127601).
912
- 913 [77] A. Agarwala, V. Juričić and B. Roy, *Higher-order topological insulators in amorphous solids*, Phys. Rev. Res. **2**, 012067 (2020), doi:[10.1103/PhysRevResearch.2.012067](https://doi.org/10.1103/PhysRevResearch.2.012067).
914
- 915 [78] J.-H. Wang, Y.-B. Yang, N. Dai and Y. Xu, *Structural-disorder-induced second-order topological insulators in three dimensions*, Phys. Rev. Lett. **126**, 206404 (2021),
916 doi:[10.1103/PhysRevLett.126.206404](https://doi.org/10.1103/PhysRevLett.126.206404).
917
- 918 [79] Y.-L. Tao, J.-H. Wang and Y. Xu, *Average symmetry protected higher-order topological amorphous insulators*, SciPost Phys. **15**, 193 (2023),
919 doi:[10.21468/SciPostPhys.15.5.193](https://doi.org/10.21468/SciPostPhys.15.5.193).
920
- 921 [80] Y.-B. Yang, J.-H. Wang, K. Li and Y. Xu, *Higher-order topological phases in crystalline and non-crystalline systems: a review*, Journal of Physics: Condensed Matter **36**(28),
922 283002 (2024), doi:[10.1088/1361-648X/ad3abd](https://doi.org/10.1088/1361-648X/ad3abd).
923

- 924 [81] M. Nakahara, *Geometry, topology and physics*, CRC press (2018).
- 925 [82] N. Marzari and D. Vanderbilt, *Maximally localized generalized Wannier functions for com-*
926 *posite energy bands*, Phys. Rev. B **56**, 12847 (1997), doi:[10.1103/PhysRevB.56.12847](https://doi.org/10.1103/PhysRevB.56.12847).
- 927 [83] N. Marzari, A. A. Mostofi, J. R. Yates, I. Souza and D. Vanderbilt, *Maximally local-*
928 *ized Wannier functions: Theory and applications*, Rev. Mod. Phys. **84**, 1419 (2012),
929 doi:[10.1103/RevModPhys.84.1419](https://doi.org/10.1103/RevModPhys.84.1419).
- 930 [84] A. A. Soluyanov and D. Vanderbilt, *Wannier representation of Z_2 topological insulators*,
931 Phys. Rev. B **83**, 035108 (2011), doi:[10.1103/PhysRevB.83.035108](https://doi.org/10.1103/PhysRevB.83.035108).
- 932 [85] C. Brouder, G. Panati, M. Calandra, C. Mourougane and N. Marzari, *Exponential lo-*
933 *calization of Wannier functions in insulators*, Phys. Rev. Lett. **98**, 046402 (2007),
934 doi:[10.1103/PhysRevLett.98.046402](https://doi.org/10.1103/PhysRevLett.98.046402).
- 935 [86] E. Prodan, *On the generalized Wannier functions*, J. Math. Phys. **56**(11), 113511 (2015),
936 doi:[10.1063/1.4936303](https://doi.org/10.1063/1.4936303).
- 937 [87] H. D. Cornean, I. Herbst and G. Nenciu, *On the construction of composite Wannier*
938 *functions*, Annales Henri Poincaré **17**(12), 3361 (2016), doi:[10.1007/s00023-016-](https://doi.org/10.1007/s00023-016-0489-2)
939 [0489-2](https://doi.org/10.1007/s00023-016-0489-2).
- 940 [88] D. Fiorenza, D. Monaco and G. Panati, *Construction of real-valued localized com-*
941 *posite wannier functions for insulators*, Annales Henri Poincaré **17**(1), 63 (2016),
942 doi:[10.1007/s00023-015-0400-6](https://doi.org/10.1007/s00023-015-0400-6).
- 943 [89] T. M. Gunawardana, A. M. Turner and R. Barnett, *Optimally localized single-band Wan-*
944 *nier functions for two-dimensional Chern insulators*, Phys. Rev. Res. **6**, 023046 (2024),
945 doi:[10.1103/PhysRevResearch.6.023046](https://doi.org/10.1103/PhysRevResearch.6.023046).
- 946 [90] D. Monaco, G. Panati, A. Pisante and S. Teufel, *Optimal decay of Wannier functions in*
947 *Chern and quantum Hall insulators*, Communications in Mathematical Physics **359**(1),
948 61 (2018), doi:[10.1007/s00220-017-3067-7](https://doi.org/10.1007/s00220-017-3067-7).
- 949 [91] J. Zhu, Z. Chen and B. Wu, *Construction of Wannier functions in disordered systems*
950 (2015), [1512.02043](https://arxiv.org/abs/1512.02043).
- 951 [92] J. C. Slater and G. F. Koster, *Simplified LCAO method for the periodic potential problem*,
952 Phys. Rev. **94**, 1498 (1954), doi:[10.1103/PhysRev.94.1498](https://doi.org/10.1103/PhysRev.94.1498).
- 953 [93] D. Li, M. Pan, C. Wang and H. Huang, *Angular momentum invoked band inversions*
954 *in mirror symmetry protected topological states*, Phys. Rev. B **105**, 195133 (2022),
955 doi:[10.1103/PhysRevB.105.195133](https://doi.org/10.1103/PhysRevB.105.195133).
- 956 [94] W. A. Harrison, *Electronic structure and the properties of solids: the physics of the chemical*
957 *bond*, Courier Corporation (2012).
- 958 [95] T. Takagi, *On an algebraic problem related to an analytic theorem of Carathéodory and Fe-*
959 *jér and on an allied theorem of Landau*, In *Japanese journal of mathematics: transactions*
960 *and abstracts*, vol. 1, pp. 83–93. The Mathematical Society of Japan (1924).
- 961 [96] P. M. Lenggenhager, X. Liu, T. Neupert and B. Tomas, *Universal higher-order bulk-*
962 *boundary correspondence of triple nodal points*, Phys. Rev. B **106**, 085129 (2022),
963 doi:[10.1103/PhysRevB.106.085129](https://doi.org/10.1103/PhysRevB.106.085129).

- 964 [97] W. J. Jankowski, M. Noormandipour, A. Bouhon and R.-J. Slager, *Disorder-induced topological quantum phase transitions in Euler semimetals* (2023), [2306.13084](https://doi.org/10.1038/s41467-024-47467-2).
965
- 966 [98] F.-J. Wang, Z.-Y. Xiao, R. Queiroz, B. A. Bernevig, A. Stern and Z.-D. Song, *Anderson critical metal phase in trivial states protected by average magnetic crystalline symmetry*,
967 Nature Communications **15**(1), 3069 (2024), doi:[10.1038/s41467-024-47467-2](https://doi.org/10.1038/s41467-024-47467-2).
968
- 969 [99] H. Huang and F. Liu, *A unified view of topological phase transition in band theory*, Research
970 **2020**, 7832610 (2020), doi:[10.34133/2020/7832610](https://doi.org/10.34133/2020/7832610).
- 971 [100] X. Ni, H. Huang and F. Liu, *Robustness of topological insulating phase against vacancy, vacancy cluster, and grain boundary bulk defects*, Phys. Rev. B **101**, 125114 (2020),
972 doi:[10.1103/PhysRevB.101.125114](https://doi.org/10.1103/PhysRevB.101.125114).
973
- 974 [101] C. Wang, T. Cheng, Z. Liu, F. Liu and H. Huang, *Structural amorphization-induced topological order*,
975 Phys. Rev. Lett. **128**, 056401 (2022),
976 doi:[10.1103/PhysRevLett.128.056401](https://doi.org/10.1103/PhysRevLett.128.056401).
- 977 [102] J. Langbehn, Y. Peng, L. Trifunovic, F. von Oppen and P. W. Brouwer, *Reflection-symmetric second-order topological insulators and superconductors*, Phys. Rev. Lett. **119**, 246401
978 (2017), doi:[10.1103/PhysRevLett.119.246401](https://doi.org/10.1103/PhysRevLett.119.246401).
979
- 980 [103] A. Bouhon and R.-J. Slager, *Multi-gap topological conversion of Euler class via band-node braiding: minimal models, PT-linked nodal rings, and chiral heirs* (2022), [2203.16741](https://doi.org/10.1038/s41467-024-47467-2).
981
- 982 [104] M. J. Park, Y. Kim, G. Y. Cho and S. Lee, *Higher-order topological insulator in twisted bilayer graphene*, Phys. Rev. Lett. **123**, 216803 (2019),
983 doi:[10.1103/PhysRevLett.123.216803](https://doi.org/10.1103/PhysRevLett.123.216803).
984
- 985 [105] E. Lee, R. Kim, J. Ahn and B.-J. Yang, *Two-dimensional higher-order topology in monolayer graphdiyne*, npj Quantum Materials **5**(1), 1 (2020), doi:[10.1038/s41535-019-0206-8](https://doi.org/10.1038/s41535-019-0206-8).
986
987
- 988 [106] X.-L. Sheng, C. Chen, H. Liu, Z. Chen, Z.-M. Yu, Y. X. Zhao and S. A. Yang, *Two-dimensional second-order topological insulator in graphdiyne*, Phys. Rev. Lett. **123**,
989 256402 (2019), doi:[10.1103/PhysRevLett.123.256402](https://doi.org/10.1103/PhysRevLett.123.256402).
990
- 991 [107] M. Pan and H. Huang, *Phononic stiefel-whitney topology with corner vibrational modes in two-dimensional xenes and ligand-functionalized derivatives*, Phys. Rev. B **106**, L201406
992 (2022), doi:[10.1103/PhysRevB.106.L201406](https://doi.org/10.1103/PhysRevB.106.L201406).
993
- 994 [108] M. Pan, D. Li, J. Fan and H. Huang, *Two-dimensional Stiefel-Whitney insulators in liganded Xenes*, npj Comput. Mater. **8**, 1 (2022), doi:[10.1038/s41524-021-00695-2](https://doi.org/10.1038/s41524-021-00695-2).
995